

Magmatic channelization by reactive and shear-driven instabilities at mid-ocean ridges: a combined analysis

D. W. Rees Jones^{1,2}, H. Zhang^{2,3} and R. F. Katz²

¹University of St Andrews, School of Mathematics and Statistics, Mathematical Institute, North Haugh, St Andrews, KY16 9SS, United Kingdom. E-mail: david.reesjones@st-andrews.ac.uk

²University of Oxford, Department of Earth Sciences, South Parks Road, Oxford, OX1 3AN, United Kingdom

³Peking University, Department of Mechanics and Engineering Science, Beijing 100871, China

Accepted 2021 March 19. Received 2021 March 19; in original form 2020 August 31

SUMMARY

It is generally accepted that melt extraction from the mantle at mid-ocean ridges (MORs) is concentrated in narrow regions of elevated melt fraction called channels. Two feedback mechanisms have been proposed to explain why these channels grow by linear instability: shear flow of the partially molten mantle and reactive flow of the ascending magma. These two mechanisms have been studied extensively, in isolation from each other, through theory and laboratory experiments as well as field and geophysical observations. Here, we develop a consistent theory that accounts for both proposed mechanisms and allows us to weigh their relative contributions. We show that interaction of the two feedback mechanisms is insignificant and that the total linear growth rate of channels is well-approximated by summing their independent growth rates. Furthermore, we explain how their competition is governed by the orientation of channels with respect to gravity and mantle shear. By itself, analysis of the reaction-infiltration instability predicts the formation of tube-shaped channels. We show that with the addition of even a small amount of extension in the horizontal, the combined instability favours tabular channels, consistent with the observed morphology of dunite bodies in ophiolites. We apply the new theory to MORs by calculating the accumulated growth and rotation of channels along streamlines of the solid flow. We show that reactive flow is the dominant instability mechanism deep beneath the ridge axis, where the most unstable orientation of high-porosity channels is subvertical. Channels are then rotated by the solid flow away from the vertical. The contribution of the shear-driven instability is confined to the margins of the melting region. Within the limitations of our study, the shear-driven feedback does not appear to be responsible for significant melt focusing or for the shallowly dipping seismic anisotropy that has been obtained by seismic inversions.

Key words: Permeability and porosity; Instability analysis; Mechanics, theory, and modelling; Mid-ocean ridge processes; Rheology: mantle.

1 INTRODUCTION

At mid-ocean ridges (MORs), plate spreading induces upwelling of the mantle, causing decompression melting. This melting occurs inside a volume (the melting region) that extends to a depth and distance of order 100 km from the ridge axis. The rock within the volume is partially molten, consisting of a crystalline solid with liquid melt along the boundaries of solid grains. The melt resides in an interconnected, permeable network of pores, such that it can segregate from the residue and migrate over large distances, driven by buoyancy and pressure gradients. Several lines of evidence suggest that the migration is not spatially uniform, but is rather localized in channels of elevated melt fraction (porosity).

A key line of evidence for channelized transport comes from geological observations of tabular bodies of nearly pure olivine (dunite) in ophiolites, which are otherwise dominantly of olivine+pyroxene lithology (harzburgite). These have been interpreted as the relics of former channels in which focused melt flow has dissolved all pyroxene and replaced it with olivine (Quick 1982; Kelemen 1990; Kelemen *et al.* 1995a, 1997, 2000; Braun & Kelemen 2002). Similar features are observed in laboratory experiments in which Si-undersaturated melts are forced to traverse a porous, olivine+pyroxene matrix (Pec *et al.* 2015, 2017). Furthermore, there is well-documented chemical disequilibrium between erupted lavas and the harzburgitic uppermost mantle. This surprising observation can be reconciled by channelized flow; transport through dunite

channels isolates rising melts from the surrounding mantle harzburgite (Kelemen *et al.* 1995a). Moreover, young lavas are typically found to contain isotopes of the uranium-series decay chain with disequilibrium activity ratios (Sims *et al.* 2002). This has been interpreted to indicate rapid melt transport from depth in the mantle, which would be a consequence of the hypothetically channelized flow (Jull *et al.* 2002; Elliott & Spiegelman 2014).

Physical models and laboratory experiments point to two possible types of fluid-mechanical instability that can cause localization of magmatic flow. First, chemical reactions during magmatic ascent can dissolve the host rock due to a solubility gradient, driving a reaction-infiltration instability (Kelemen 1990; Aharonov *et al.* 1995; Kelemen *et al.* 1995b). Second, shear of the solid rock coupled with the fact that its viscous strength decreases with melt fraction cause a shear-driven banding instability (Stevenson 1989; Holtzman *et al.* 2003a). These mechanisms have been extensively studied in isolation, and their outcomes have been invoked separately to explain natural observations.

The key objective of the present paper is to assess the relative contributions of these two instabilities to melt transport within the MOR melting region. In particular, it is to discover the dynamic and parametric conditions under which the shear-driven instability can contribute significantly to the overall pattern of channelized melt transport. It has been widely assumed that the shear-driven instability makes an important contribution to melt flow and mantle dynamics (e.g. Kohlstedt & Holtzman 2009; Kawakatsu *et al.* 2009; Holtzman & Kendall 2010), but no quantitative assessment that also includes reactive flow has been published. In the context of our simplified analysis, we test and ultimately challenge this assumption. Instead we argue that the reaction-infiltration instability is dominant and that shear-driven instability may be insignificant beneath MORs.

We reviewed research into the reaction-infiltration instability in Rees Jones & Katz (2018) and augment that review briefly here. Recent laboratory experiments at high temperature and pressure showed that highly permeable, cylindrical conduits form due to the reactive flow of Si-undersaturated melt (Pec *et al.* 2015, 2017, 2020). Similar cylindrical features also arise from reactive instabilities in a class of porous media called mushy layers (Tait *et al.* 1992; Worster 1997). The cylindrical geometry of channels in mushy layers is noteworthy because it contrasts with the tabular nature of dunite bodies in ophiolites. Theoretical work has focused on linear stability analysis and 2-D numerical calculations (Aharonov *et al.* 1995; Spiegelman *et al.* 2001; Hewitt 2010; Liang *et al.* 2010; Hesse *et al.* 2011; Schiemenz *et al.* 2011; Szymczak & Ladd 2013, 2014; Jordan & Hesse 2015). Numerical calculations of reactive flow were extended by Baltzell *et al.* (2015) to include the effect of mantle shear. However, that study used a constant shear viscosity rather than one that is porosity-weakening. Thus it considered the effect of shear in stretching and rotating high-porosity features caused by the reactive instability, but excluded the potential for the shear flow to drive a melt-localizing instability.

The shear-driven instability was reviewed by Kohlstedt & Holtzman (2009). The instability was predicted theoretically by Stevenson (1989) before being confirmed experimentally by Holtzman *et al.* (2003a). It has since been the subject of extensive laboratory experiments (Holtzman & Kohlstedt 2007; King *et al.* 2011b; Qi *et al.* 2015) and theoretical study (Spiegelman 2003; Katz *et al.* 2006; Butler 2009; Alisic *et al.* 2016). Recent consensus is that it is controlled by viscous anisotropy (Takei & Holtzman 2009a,b,c; Butler 2012; Takei & Katz 2013; Katz & Takei 2013; Qi *et al.* 2015), although the details remain incompletely understood. The emergent

patterns, including the associated development of a distinct mode of olivine lattice preferred orientation (Holtzman *et al.* 2003b) and hence seismic anisotropy (Holtzman & Kendall 2010), have been invoked to explain proxy measurements.

A set of laboratory experiments reported by King *et al.* (2011c) considered the combined role of reaction and shear in generating melt bands. However, the experimental conditions are so far from the natural system that it is difficult to draw general conclusions from that study.

The natural system of primary interest here is the MOR. MORs are a fundamental component of plate tectonics, the predominant locus of present terrestrial magmatism, and a context in which melt channelization is inferred from observations, as discussed above. The stability analysis of Butler (2009) suggested that shear-driven porosity bands would form here. However, that study neglected the role of buoyancy and ongoing melting. Vestrum & Butler (2020) considered the effect of both buoyancy and a uniform background melting rate (but excluded reactive melting). They showed that the consequences of uniform melting depend on details of the rheological model. Furthermore, they showed that buoyancy does not affect the magnitude of the shear bands; rather, it causes bands to travel as porosity waves. These studies cannot, however, address the relative importance of reactive flow to melt localization. The relative importance was tested in terms of its geochemical consequences by Liu & Liang (2019), who considered models with various distributions of both reactive channels and shear-induced bands. However, the distribution and character of localized porosity features in Liu & Liang (2019) were prescribed, rather than emerging dynamically.

The broad goal of this paper is to develop a theoretical understanding of the combined dynamics of reactive and shear-driven instabilities in the partially molten upper mantle. This allows us to assess their relevance for magmatic flow localization at MORs, at length- and timescales that are necessarily very different from those of the laboratory. Insights gained here may have wider implications for magmatism.

In Section 2, we develop a theoretical method to determine the linear growth rate of perturbations in the form of alternating bands of higher and lower porosity. The theory allows for the perturbations to evolve by both reactive and shear mechanisms simultaneously. We show that this theory can reproduce previous estimates of their growth rate in both the reaction-only and shear-only limits.

In Section 3, we apply this theory to the idealized scenario of an infinite, partially molten material with a uniform background magmatic flow, a linear solubility gradient aligned with gravity, and a linear shear of the solid matrix. We identify a parameter that describes the relative importance of reaction and shear. In this idealized context we show that there are two distinguished directions that control the orientation of high-porosity pathways: one in the direction of gravity (the vertical) over which there is a chemical solubility gradient, and the other in the direction of the maximum tensile deviatoric stress. We calculate the growth of the instability and show that the optimal orientation for growth of porosity perturbations depends on these directions and also the ratio of shear-to-reactive growth rates. Indeed, within a plane normal to gravity, it is shear that breaks the horizontal isotropy. We show that the most unstable, fastest growing features are tabular bodies extending horizontally in the direction in which there is no component of the shear flow. This is important because dunites are observed to be tabular features, rather than the cylindrical conduits favoured by the pure reaction-infiltration instability. In this section we also discuss the role of compaction, chemical advection and diffusion, all of which play a role in determining the wavelength-dependence of the growth rate.

Table 1. State variables and selected formulae.

Symbol	Property
(x, y, z)	Cartesian co-ordinates
t	Time
ϕ	Porosity
Γ	Volumetric melt rate
\mathbf{v}_s	Solid velocity: $\mathbf{v}_s = \mathbf{u} + \nabla U$
\mathbf{u}	Divergence-free part of solid velocity
∇U	Curl-free part of solid velocity
\mathbf{v}_l	Liquid velocity
\mathbf{v}_D	Darcy velocity: $\phi(\mathbf{v}_l - \mathbf{v}_s)$
\mathcal{C}	Compaction rate: $\mathcal{C} = \nabla \cdot \mathbf{v}_s$
\mathbf{D}_s	Deviatoric strain rate: $\mathbf{D}_s = \frac{1}{2} \left[\nabla \mathbf{v}_s + \nabla \mathbf{v}_s^T - \frac{2}{3} \mathcal{C} \mathbf{I} \right]$
P_l	Liquid pressure
c_l	Liquid concentration
X	Liquid undersaturation

In Section 4, we present a methodology and in Section 5 we present results from the first combined assessment of both reactive and shear-driven instability at MORs. We build on the approach of Gebhardt & Butler (2016), allowing the amplitude and orientation of perturbations to evolve along streamlines of the solid flow, based on their local growth rate. But whereas Gebhardt & Butler (2016) considered only shear-driven growth, in our case, the growth rate is a consequence of both reaction and shear. We show that their contributions are not spatially uniform and predict how they vary along corner-flow streamlines. Generally, we find that the initial growth of porosity bands is dominated by reaction. Within the space of the melting region and the plausible ranges of control parameters, our results indicate that melt channels are subvertical features that undergo some rotation by the shear flow. Shear-driven instability is predicted to contribute at the margins of the melting region.

In Section 6, we review the implications of these findings for understanding the relative importance of reaction and shear in driving channelized melt extraction from the mantle. We discuss implications for interpreting the origins of tabular dunites embedded in a harzburgitic upper mantle. We also discuss melt focusing towards the ridge axis, as well as seismic anisotropy that has been attributed to aligned, melt-rich bands.

2 METHODS: LOCAL ANALYSIS OF COMBINED INSTABILITY

2.1 Equations governing two-phase flow

The partially molten upper mantle can be modelled as a region of two-phase flow. The continuum model that we use, developed by McKenzie (1984), is based on averaging all the quantities of interest across a control volume containing both solid and liquid phase. Table 1 lists the state variables and Table 2 lists the physical properties that we define in this section. Our formulation makes a Boussinesq approximation: the solid density ρ_s and liquid density ρ_l are taken to be constants, and their difference $\Delta\rho = \rho_s - \rho_l$ is neglected everywhere, except in so far as it drives segregation of the liquid by buoyancy.

Mass conservation in the liquid phase is given by

$$\frac{\partial\phi}{\partial t} + \nabla \cdot (\phi \mathbf{v}_l) = \Gamma, \quad (1)$$

where t is time, ϕ is the porosity, \mathbf{v}_l is the liquid velocity and Γ is the volumetric melting rate. Similarly, mass conservation in the

Table 2. Physical properties and selected formulae.

Symbol	Property
ρ_s	Density of solid
ρ_l	Density of liquid
$\Delta\rho$	Density difference: $\Delta\rho = \rho_s - \rho_l$
$\bar{\rho}$	Bulk density: $\bar{\rho} = \phi\rho_l + (1 - \phi)\rho_s$
\mathbf{g}	Gravity vector
g	Gravitational acceleration: $g = \mathbf{g} $
K	Fluid mobility (permeability/fluid viscosity)
η	Shear viscosity
ζ	Bulk viscosity
R	Reaction rate constant
α	Inverse reactivity
β	Equilibrium concentration gradient
D_X	Chemical diffusivity in liquid phase

solid phase is given by

$$\frac{\partial(1 - \phi)}{\partial t} + \nabla \cdot ((1 - \phi)\mathbf{v}_s) = -\Gamma, \quad (2)$$

where \mathbf{v}_s is the solid velocity. The compaction rate is defined as $\mathcal{C} = \nabla \cdot \mathbf{v}_s$. It is convenient to sum eqs (1) and (2) to form an equation for the compaction rate:

$$\mathcal{C} + \nabla \cdot \mathbf{v}_D = 0, \quad (3)$$

where the Darcy (melt segregation) velocity is defined as

$$\mathbf{v}_D \equiv \phi(\mathbf{v}_l - \mathbf{v}_s). \quad (4)$$

Then eq. (2) can be rewritten

$$\frac{\partial\phi}{\partial t} + \mathbf{v}_s \cdot \nabla\phi = \Gamma + (1 - \phi)\mathcal{C}. \quad (5)$$

In this formulation, porosity, moving with the solid phase, evolves due to melting rate Γ and compaction \mathcal{C} . Note that $\mathcal{C} > 0$ represents a decompaction of the mantle matrix, that is, an increase in the porosity. Eqs (3) and (5) define two-phase mass conservation in our system.

Next, two-phase momentum conservation can be written using a ‘Stokes–Darcy’ formulation. The Darcy velocity

$$\mathbf{v}_D = -K(\nabla P_l - \rho_l \mathbf{g}) \quad (6)$$

is driven by gradients in the liquid pressure P_l and buoyancy (\mathbf{g} is gravity). K is the liquid mobility, which is defined as the permeability divided by the liquid viscosity. We will often refer to K as the permeability, since we assume the liquid viscosity is a constant so variation in K comes from variation in permeability. The Stokes part of the system can be written

$$\nabla P_l = \nabla \cdot [2\eta \mathbf{D}_s] + \nabla(\zeta \mathcal{C}) + \bar{\rho} \mathbf{g}, \quad (7)$$

where η is the shear viscosity (Newtonian), ζ is the bulk viscosity, $\bar{\rho} = \phi\rho_l + (1 - \phi)\rho_s = \rho_l + (1 - \phi)\Delta\rho$ is the bulk density and

$$\mathbf{D}_s = \frac{1}{2} \left[\nabla \mathbf{v}_s + \nabla \mathbf{v}_s^T - \frac{2}{3} \mathcal{C} \mathbf{I} \right] \quad (8)$$

is the deviatoric strain rate tensor (\mathbf{I} is the identity tensor, T is the transpose operator).

We discuss constitutive laws and the dependence of material properties on porosity in the next section. For now, we note that the shear-driven mode of instability relies on the fact that η decreases with ϕ . This motivates expanding out the derivatives involving η . We also apply a Helmholtz decomposition of the solid velocity into a shearing (incompressible) part and a compacting (compressible,

but irrotational) part

$$\mathbf{v}_s = \mathbf{u} + \nabla U, \quad \nabla \cdot \mathbf{u} = 0, \quad (9)$$

where U is a scalar potential that can be related to \mathcal{C} by the relationship $\mathcal{C} = \nabla^2 U$. Then eq. (7) becomes:

$$\nabla P_l = 2\mathbf{D}_s \cdot \nabla \eta + \eta \nabla^2 \mathbf{u} + \frac{4}{3} \eta \nabla \mathcal{C} + \nabla(\zeta \mathcal{C}) + \bar{\rho} \mathbf{g}. \quad (10)$$

The terms involving pressure, $\eta \nabla^2 \mathbf{u}$ and gravity can be recognized as the usual, single-phase form of Stokes law with a constant Newtonian viscosity. We can eliminate various terms by taking the curl of eq. (10) to form a type of vorticity equation

$$0 = \nabla \times \left[2\mathbf{D}_s \cdot \nabla \eta + \eta \nabla^2 \mathbf{u} + \frac{4}{3} \eta \nabla \mathcal{C} - \phi \Delta \rho \mathbf{g} \right]. \quad (11)$$

We can also substitute eq. (10) into eq. (6) to obtain

$$\mathbf{v}_D = -K \left[2\mathbf{D}_s \cdot \nabla \eta + \eta \nabla^2 \mathbf{u} + \frac{4}{3} \eta \nabla \mathcal{C} + \nabla(\zeta \mathcal{C}) + (1 - \phi) \Delta \rho \mathbf{g} \right]. \quad (12)$$

The melting rate Γ is determined by chemical disequilibrium. We describe the model that we and others have used in more detail in Rees Jones & Katz (2018); the original model is due to Aharonov *et al.* (1995). The crucial ingredients are that the melting rate is linearly proportional to the chemical disequilibrium

$$\Gamma = R X, \quad (13)$$

where R is the reaction rate constant and X is the chemical undersaturation. That R is constant is a reasonable assumption during the initial growth of the instability; later R will decrease as the concentration of the soluble component in the solid phase decreases. Eq. (13) is a first order, linear, kinetic reaction rate equation. Then X is governed by an advection–diffusion–reaction equation, which can be written in the form

$$-\phi \frac{\partial X}{\partial t} + \phi \mathbf{v}_l \cdot \nabla (\beta z - X) = \alpha \Gamma - \nabla \cdot (\phi D_X \nabla X), \quad (14)$$

where β is the constant gradient of the equilibrium chemical concentration, sometimes called the solubility gradient, which we assume is orientated in the vertical direction. Under these assumptions, the liquid concentration can be written in terms of the undersaturation as $c_l = \beta z - X$, appearing in the second term in eq. (14). Also, α represents the supersaturation of the reactively produced melts that drive the system back towards equilibrium. Within eq. (14), α is an inverse reactivity, because the reactive melt rate Γ is inversely proportional to α . Finally, D_X is the diffusivity of chemical species in the liquid phase, scaled by the porosity ϕ . Diffusion in the liquid is much faster than that in the solid, so diffusivity of chemical species in the solid phase is neglected.

All the approximations made here are described in more detail in Rees Jones & Katz (2018). For now we focus on the equilibrium concentration gradient because this drives the reactive instability. In a more complete description, the equilibrium chemical concentration depends on pressure (Kelemen *et al.* 1995b; Longhi 2002). Thus this simple formulation with constant β combines an assumption that the pressure is dominantly lithostatic, that is, proportional to vertical position z , and an assumption that the dependence of equilibrium chemical concentration on pressure is linear. The latter assumption could be relaxed straightforwardly by allowing β to vary with z . In Appendix A, we consider the full pressure-dependence of the equilibrium concentration gradient and hence the reactive melting rate. The shear-driven instability creates a pressure gradient that can, in turn, feed back on the reactive instability through the

pressure-dependent reactive melt rate. So Appendix A also considers this mode of coupling between the two types of instability. We find the effects of the pressure-dependence on the linear growth rate of the reactive instability are relatively small, because $\Delta \rho / \rho_s \ll 1$, which means that the pressure is dominantly lithostatic. However, it is possible that the pressure-dependence may have a larger effect on the nonlinear development of channels. Spiegelman *et al.* (2001) suggested that lateral pressure gradients that focus flow towards a mid-ocean-ridge (MOR) axis could promote the development of a diagonal solubility gradient that would further enhance convergence of flow towards the ridge axis. Nonlinear calculations extending those of Spiegelman *et al.* (2001) could assess the significance of this proposed mechanism at MORs.

In the upper mantle, porosity is typically very small, so we can further simplify these equations by making the approximations $(1 - \phi) \approx 1$, $\phi \mathbf{v}_l \approx \mathbf{v}_D$, and neglecting the terms $\mathbf{v}_s \cdot \nabla \phi \ll 1$, $\phi \frac{\partial X}{\partial t} \ll 1$ and $\nabla \times \phi \Delta \rho \mathbf{g}$. We will revisit the role of porosity advection $\mathbf{v}_s \cdot \nabla \phi$ later (Section 4.2.1). We can also eliminate the undersaturation X using eq. (13). Under these approximations, we obtain a system of equations that includes the physical mechanisms that give rise to both shear and reaction driven instabilities:

$$\frac{\partial \phi}{\partial t} = \Gamma + \mathcal{C}, \quad (15)$$

$$\mathcal{C} + \nabla \cdot \mathbf{v}_D = 0 \quad (16)$$

$$0 = \nabla \times \left[2\mathbf{D}_s \cdot \nabla \eta + \eta \nabla^2 \mathbf{u} + \frac{4}{3} \eta \nabla \mathcal{C} \right], \quad \nabla \cdot \mathbf{u} = 0, \quad (17)$$

$$\mathbf{v}_D = -K \left[2\mathbf{D}_s \cdot \nabla \eta + \eta \nabla^2 \mathbf{u} + \frac{4}{3} \eta \nabla \mathcal{C} + \nabla(\zeta \mathcal{C}) + \Delta \rho \mathbf{g} \right]. \quad (18)$$

$$\mathbf{v}_D \cdot \nabla (\beta z - R^{-1} \Gamma) = \alpha \Gamma - \nabla \cdot (\phi D_X R^{-1} \nabla \Gamma). \quad (19)$$

2.2 Equations governing linear growth of instabilities

Our first goal is to determine the local growth rate of instabilities about a uniform background state with a linear incompressible shear flow \mathbf{u} and a vertical Darcy flow $w_{D0} \hat{\mathbf{z}}$, where $\hat{\mathbf{z}}$ is a unit vector in the z -direction. We write all the fields as an expansion into a base state (subscript 0) and a perturbation ($'$)

$$\begin{aligned} \phi &= \phi_0 + \phi', & \mathcal{C} &= \mathcal{C}_0 + \mathcal{C}', & \Gamma &= \Gamma_0 + \Gamma' \\ \mathbf{u} &= \mathbf{u}_0 + \mathbf{u}', & \mathbf{v}_D &= w_{D0} \hat{\mathbf{z}} + \mathbf{v}_D'. \end{aligned} \quad (20)$$

Table 3 summarizes the notation introduced in this section.

A crucial ingredient of the reactive- and shear-driven instabilities is that the constitutive laws (material properties) depend on porosity. We can linearize all the constitutive laws by expanding them in a Taylor series in ϕ truncated at first order

$$K = K_0 + K', \quad \eta = \eta_0 + \eta', \quad \zeta = \zeta_0 + \zeta', \quad (21)$$

where all the primed variables are proportional to ϕ' . For example

$$K(\phi_0 + \phi') = K(\phi_0) + \phi' \left. \frac{dK}{d\phi} \right|_{\phi=\phi_0} \equiv K_0 + K'. \quad (22)$$

A common choice of constitutive law for permeability, and hence melt mobility assuming melt viscosity is constant, is $K = K^* \phi^n$, where K^* is a material property and n is an exponent (e.g. von Bargen & Waff 1986). Then

$$K_0 = K^* \phi_0^n, \quad K' = n K_0 \phi' / \phi_0. \quad (23)$$

Likewise for shear viscosity, a commonly used law is $\eta = \eta_0 \exp[-\lambda^*(\phi - \phi_0)]$, where λ^* is a material property (e.g.

Table 3. Selected additional variables arising in linear stability analysis.

Symbol	Property
σ	Growth rate of normal modes
\mathbf{k}	Wavevector of normal modes
k	Amplitude of wavevector (wavenumber)
(k_x, k_y, k_z)	Cartesian components of wavevector
(θ, ψ)	Spherical polar components of wavevector
0	Background component
$'$	Perturbation component
w_{D0}	Background Darcy velocity
w_0	Background liquid velocity
$\dot{\gamma}_0$	Background strain rate
θ_e	Angle of maximum extension
$\psi', (\tilde{\psi}')$	Scalar potential, (scaled)
λ^*	Sensitivity of shear viscosity to porosity
n	Exponent in porosity–permeability relationship
δ	Compaction length: $\delta = \sqrt{K_0 \left(\frac{4}{3} \eta_0 + \zeta_0 \right)}$
Λ	Shear-driven instability scale: $\Lambda = 2K_0 \eta_0 \lambda^* \dot{\gamma}_0$
Da_w, Da_D	Damköhler numbers
G	Angular dependence of growth rate
σ_{shear}	Growth rate of shear-driven instability: $\sigma_{\text{shear}} = \Lambda/\delta^2$
σ_{reaction}	Growth rate of reaction-driven instability: $\sigma_{\text{reaction}} = n\beta w_0/\alpha$
S	Growth rate ratio: $S = \sigma_{\text{shear}}/\sigma_{\text{reaction}}$

Kelemen *et al.* 1997; Mei *et al.* 2002). Then

$$\eta' = -\lambda^* \eta_0 \phi'. \quad (24)$$

The same methodology can be applied to any form of constitutive law that has a continuous first derivative. We do not state any particular constitutive law for the bulk viscosity at this stage, because ζ' does not affect the linear analysis that follows. We discuss this issue further in Section 4.1.2.

2.2.1 Background state

We are interested in the development of perturbations to an initially uniform porosity field with a uniform, background upward flow of magma and a linear, incompressible mantle shear flow. This state is called the background or base state.

A somewhat subtle issue is that a uniform background state is only an approximate solution of eqs (16)–(19). In Rees Jones & Katz (2018), we showed that this approximation holds provided we are dealing with length scales much smaller than $\alpha\beta^{-1} \approx 500$ km. Physically, the system is only weakly reactive. In this approximation, the background compaction rate is negligible, so $C_0 = 0$. This approximation is equivalent to saying that the background melting rate (which balances the background compaction rate) is negligible, an issue we discuss later in the context of MORs (Section 4.1.2).

Eq. (18) gives an expression for the background Darcy velocity that can also be written in terms of the liquid velocity w_0 using $w_{D0} = \phi_0 w_0$. In particular,

$$w_{D0} = K_0 \Delta \rho g, \quad w_0 = \frac{K_0 \Delta \rho g}{\phi_0}, \quad g = |\mathbf{g}|. \quad (25)$$

Any linear incompressible shear flow satisfies eq. (17), because $\nabla \eta = 0$ and $\nabla C = 0$. We define

$$\mathbf{D}_0 = \frac{1}{2} [\nabla \mathbf{u}_0 + \nabla \mathbf{u}_0^T], \quad (26)$$

which is the symmetric velocity gradient tensor associated with the background shear flow (note this is a constant and trace-free tensor,

because the background shear flow is linear and incompressible). A MOR far from any offsets is roughly 2-D, so if we choose the x -axis to be in the direction of plate spreading, the shear is in the x - z plane. Then a general expression for the symmetric velocity gradient tensor of this type of flow is

$$\mathbf{D}_0 = \dot{\gamma}_0 \tilde{\mathbf{D}}_0, \quad \tilde{\mathbf{D}}_0 = \begin{bmatrix} \cos(2\theta_e) & 0 & \sin(2\theta_e) \\ 0 & 0 & 0 \\ \sin(2\theta_e) & 0 & -\cos(2\theta_e) \end{bmatrix}, \quad (27)$$

where $\dot{\gamma}_0$ is the background strain rate and θ_e is the angle of maximum extension ($\theta_e = 0$ corresponds to extension in the x -direction and $\theta_e = \pi/2$ corresponds to extension in the z -direction). By this choice of co-ordinates, there is no extension or contraction in the y -direction. Equivalently, $\psi_e = 0$, where ψ is the azimuthal angle (Fig. 1).

2.2.2 Linear equations

We now substitute the linear decompositions from eqs (20)–(27) into the governing eqs (16)–(19) and neglect any quadratic terms. The vorticity eq. (17) becomes

$$0 = \nabla \times [2\mathbf{D}_0 \cdot \nabla \eta' + \eta_0 \nabla^2 \mathbf{u}'], \quad \nabla \cdot \mathbf{u}' = 0, \quad (28)$$

Here, we exploited the fact that the background compaction rate is negligible, which means that the effect of variations in bulk viscosity turn out to be consequently small [we discuss the effect of variation in bulk viscosity in Rees Jones & Katz (2018) so do not elaborate further here].

Eq. (28) motivates the introduction of a scalar potential ψ' defined by

$$\nabla \psi' = [2\mathbf{D}_0 \cdot \nabla \eta' + \eta_0 \nabla^2 \mathbf{u}'], \quad (29)$$

which (since $\nabla \cdot \mathbf{u}' = 0$) must satisfy a Poisson equation

$$\nabla^2 \psi' = 2\mathbf{D}_0 : \nabla \nabla \eta'. \quad (30)$$

Then we introduce a scaled, dimensionless potential

$$\tilde{\psi}' = \frac{\psi'}{-2\lambda^* \eta_0 \dot{\gamma}_0}, \quad \Rightarrow \quad \nabla^2 \tilde{\psi}' = \tilde{\mathbf{D}}_0 : \nabla \nabla \phi', \quad (31)$$

where the implication follows using eqs (24) and (27).

The remaining equations can be rewritten by substituting the constitutive laws and eliminating the Darcy velocity. An expression for the perturbed Darcy velocity is given in Appendix A in eq. (A14). The remaining equations become

$$\frac{\partial \phi'}{\partial t} = \Gamma' + C'. \quad (32)$$

$$0 = (1 - \delta^2 \nabla^2) C' + n w_0 \phi'_z + \Lambda \tilde{\mathbf{D}}_0 : \nabla \nabla \phi' \quad (33)$$

$$n w_0 \phi' - \delta^2 C'_z + \Lambda \tilde{\psi}'_z = \frac{1}{\beta} \left\{ \alpha + \frac{\phi_0 w_0}{R} \partial_z - \frac{\phi_0 D_X}{R} \nabla^2 \right\} \Gamma', \quad (34)$$

where a subscript z is used to denote a partial derivative with respect to z . Two important parameters emerge:

$$\delta = \sqrt{K_0 \left(\frac{4}{3} \eta_0 + \zeta_0 \right)}, \quad (35)$$

$$\Lambda = 2K_0 \eta_0 \lambda^* \dot{\gamma}_0, \quad (36)$$

where δ is the compaction length (McKenzie 1984) and Λ controls how much shear-driven compaction arises from a porosity perturbation. The ratio Λ/δ^2 determines the growth rate of the shear-driven instability (Section 2.3). This ratio was first identified by Stevenson (1989), in which it is written σ_m .

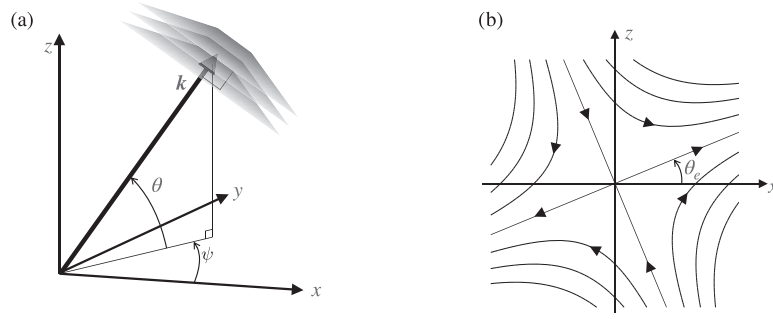


Figure 1. Sketch defining coordinates and angles. (a) The 3-D coordinate system associated with the model of instability (Section 2.1). \mathbf{k} is the wave vector, which is normal to perturbation surfaces of constant phase. These infinite, parallel surfaces are represented by shaded patches of finite extent. (b) Streamlines of the pure-shear background flow (Section 2.2.1) with the direction of extension oriented at an angle θ_e to the x -axis.

2.2.3 Normal modes

We now look for normal mode solutions of the form

$$\begin{aligned}\phi' &= \tilde{\phi} \exp(i\mathbf{k} \cdot \mathbf{x} + \sigma t), \\ \tilde{\psi}' &= \tilde{\psi} \exp(i\mathbf{k} \cdot \mathbf{x} + \sigma t), \\ C' &= \tilde{C} \exp(i\mathbf{k} \cdot \mathbf{x} + \sigma t), \\ \Gamma' &= \tilde{\Gamma} \exp(i\mathbf{k} \cdot \mathbf{x} + \sigma t),\end{aligned}$$

where σ is the growth rate of the instability, $\mathbf{k} = [k_x, k_y, k_z]$ is the wavevector, $\mathbf{x} = [x, y, z]$ is the position vector, and the prefactors are constants. We define k as the magnitude of \mathbf{k} , so $k^2 = k_x^2 + k_y^2 + k_z^2$. The co-ordinate system is shown in Fig. 1.

We define the function

$$G(\mathbf{k}; \theta_e) = k^{-2} [(k_x^2 - k_z^2) \cos(2\theta_e) + 2k_x k_z \sin(2\theta_e)], \quad (37)$$

such that eq. (31) becomes $\tilde{\psi} = \tilde{\phi} G$. The use of a factor k^{-2} in the definition ensures that G is independent of the wavenumber (magnitude of the wavevector) and only depends on the direction. G has a maximum value of +1 when $k_y = 0$ and \mathbf{k} is in the direction of maximum extension. G has a minimum value of -1 when $k_y = 0$ and \mathbf{k} is perpendicular to the direction of maximum extension. Then eqs (32)–(34) become

$$\sigma \tilde{\phi} = \tilde{\Gamma} + \tilde{C}. \quad (38)$$

$$\tilde{C} = \frac{\Lambda G k^2 - n w_0 i k_z}{1 + \delta^2 k^2} \tilde{\phi} \quad (39)$$

$$\frac{\tilde{\alpha}}{\beta} \tilde{\Gamma} = (n w_0 + i k_z \Lambda G) \tilde{\phi} - i k_z \delta^2 \tilde{C}, \quad (40)$$

where

$$\tilde{\alpha} = \alpha + \frac{\phi_0 w_0}{R} i k_z + \frac{\phi_0 D_X}{R} k^2 \quad (41)$$

is an extended version of the inverse reactivity of the system, which is augmented by advection and diffusion of the undersaturated chemical species.

Finally, we substitute eq. (40) and then eq. (39) into eq. (38) to obtain an expression for the combined growth rate of shear and reactive instabilities

$$\sigma = \frac{\beta}{\tilde{\alpha}} (n w_0 + i k_z \Lambda G) + \left(1 - \frac{\beta i k_z \delta^2}{\tilde{\alpha}}\right) \frac{\Lambda G k^2 - n w_0 i k_z}{1 + \delta^2 k^2}. \quad (42)$$

In subsequent sections, we explore the nature of this equation in detail and discuss the physical significance of the terms that appear in it. First, we relate it to previous studies of the reactive- and shear-driven instabilities in isolation.

2.3 Shear-driven instabilities

The reactive part of the growth rate can be eliminated by setting $\beta = 0$. This ensures that $\tilde{\Gamma} = 0$, so the reactive part of the contribution to porosity change is eliminated and we are left with the part coming from shear. Then eq. (42) becomes

$$\sigma = \frac{\Lambda G k^2 - n w_0 i k_z}{1 + \delta^2 k^2}. \quad (43)$$

The term involving w_0 arising from buoyancy-driven melt flow is typically neglected because buoyancy is unimportant in laboratory experiments that impose a rapid shear (Spiegelman 2003). In any case, it only affects the imaginary part of the growth rate, giving rise to compaction waves. The dependence on the compaction length δ in eq. (43) means that when $\delta k \ll 1$ (the wavelength of the instability is much greater than the compaction length), then the growth rate approaches zero. Conversely, when $\delta k \gg 1$, the real part of the growth rate can be approximated

$$\text{real}(\sigma) \approx \frac{\Lambda G}{\delta^2} = \frac{2\lambda^* \dot{\gamma}_0}{\frac{4}{3} + \frac{\zeta_0}{\eta_0}} G. \quad (44)$$

This motivates us to define

$$\sigma_{\text{shear}} = \frac{\Lambda}{\delta^2} = \frac{2\lambda^* \dot{\gamma}_0}{\frac{4}{3} + \frac{\zeta_0}{\eta_0}}, \quad (45)$$

which is the dimensional growth rate associated with shear (Steven-son 1989). Note that the real part of the growth rate has a distinguished direction, namely the direction of extension in the x - z plane. The imaginary part comes from vertical background magma flow, which drives the perturbations upward as waves. So the vertical is an additional distinguished direction in this case. The growth rate and angular dependence through eq. (37) are known from previous studies (e.g. Spiegelman 2003; Katz *et al.* 2006).

2.4 Reaction-driven instabilities

The shear part of the flow can be eliminated by taking $\Lambda = 0$. Then eq. (42) becomes

$$\sigma = \frac{1}{1 + \delta^2 k^2} \left[\frac{\beta n w_0}{\tilde{\alpha}} (1 + \delta^2 (k_x^2 + k_y^2)) - n w_0 i k_z \right]. \quad (46)$$

This can be shown to be equivalent to Rees Jones & Katz (2018) under the same assumption ($\delta k \gg 1$) mentioned previously. For now, note that if we additionally make the assumption $\tilde{\alpha} \approx \alpha$ (valid when the reaction rate R is very fast), then

$$\text{real}(\sigma) \approx \frac{\beta n w_0}{\alpha} \frac{k_x^2 + k_y^2}{k^2}. \quad (47)$$

The growth rate has a cylindrical symmetry about the vertical direction. The maximum growth rate

$$\sigma_{\text{reaction}} = n\beta w_0/\alpha, \quad (48)$$

occurs when $k_z = 0$, since $k_x^2 + k_y^2 = k^2 - k_z^2$. Thus the channels formed by the reaction-infiltration instability are vertical (Rees Jones & Katz 2018). Moreover, we show in Appendix A that the preferred vertical orientation holds even when we consider the full pressure-dependence of the solubility gradient (at least in the context of linearized analysis).

In this section, we have shown that the full dispersion relation (42) includes, as special cases, the results of previous studies on both the shear-driven instability and the reaction-infiltration instability.

3 RESULTS: LOCAL ANALYSIS OF COMBINED INSTABILITY

In this section we analyse controls on the growth rate σ that are relevant to the case of an infinite domain with a uniform base state.

3.1 Equilibrium dynamics at large compaction length

The simplest version of the instability involving both reaction and shear can be illustrated by considering an important limit of eq. (42). In particular, if the reaction rate is very fast, the system is driven to equilibrium and $\tilde{\alpha} \approx \alpha$. If also we consider the short-wavelength or large-compaction-length limit discussed earlier ($\delta k \gg 1$), then

$$\sigma = \frac{\beta}{\alpha} (nw_0 + ik_z \Lambda G) + \left(1 - \frac{\beta ik_z \delta^2}{\alpha}\right) \frac{\Lambda G k^2 - nw_0 ik_z}{\delta^2 k^2}, \quad (49)$$

so

$$\begin{aligned} \text{real}(\sigma) &= \frac{\beta nw_0}{\alpha} \left(1 - \frac{k_z^2}{k^2}\right) + \frac{\Lambda}{\delta^2} G, \\ &= \sigma_{\text{reaction}} \left(1 - \frac{k_z^2}{k^2}\right) + \sigma_{\text{shear}} G. \end{aligned} \quad (50)$$

It is important to note that all the terms involving the wavevector are independent of its magnitude; they depend only on its direction. This is a feature of the particular limit considered that (by design) neglects the role of advection, diffusion and compaction in affecting the wavelength. We consider these controls later.

In this particular limit, the behaviour is controlled by the ratio of the growth rate of shear-driven to reaction-driven instabilities, which we can write

$$S = \frac{\sigma_{\text{shear}}}{\sigma_{\text{reaction}}} = \frac{2\lambda^* \alpha}{n\beta \left(\frac{4}{3} + \frac{\xi_0}{\eta_0}\right) w_0} \dot{\gamma}_0, \quad (51)$$

where we grouped together material parameters separately to the ratio $\dot{\gamma}_0/w_0$. The former group might be expected to be roughly constant, provided the bulk-to-shear viscosity ratio is constant, whereas the latter will vary spatially at a MOR.

3.2 3-D effects and the orientation of porosity bands

The reactive mode of instability has a cylindrical symmetry (there is no difference between the x and y direction; the only distinguished direction is the vertical z). Numerical calculations show that the instability leads to the formation of cylindrical, high-porosity conduits (M. Spiegelman, unpublished work), in accordance with laboratory experiments (Pec *et al.* 2015, 2017). However, the shear-driven mode of instability leads to the formation of high-porosity sheets,

the orientation of which depends on the direction θ_e of maximum rate of extension. The coordinate system is aligned such that shear is in the x - z plane, with the direction of extension having an azimuthal angle $\psi_e = 0$ to that plane. Hence porosity sheets extend parallel to the y -direction. In cross-section on the x - z plane, the sheets appear as high-porosity bands (which is how laboratory experiments are typically presented). Here, we investigate the combined effect of the reactive and shear mechanisms in light of the fact that this combination has two distinguished directions: the orientation of the shear flow and the direction of the solubility gradient (vertical).

We work in terms of modified spherical polar co-ordinates (θ, ψ) , shown in Fig. 1(a), where $-\pi/2 \leq \theta \leq \pi/2$ is the inclination angle and $0 \leq \psi < 2\pi$ is the azimuthal angle. This definition of θ is consistent with that of θ_e (Fig. 1b). However, it is not the same as the angle of the porosity bands as it was defined in, for example, Spiegelman (2003). Rather, as shown in Fig. 1(a), the porosity bands are normal to the wavevector that makes an angle θ to the x - y plane. In the particular case that we restrict attention to the x - z plane ($\psi = 0$), the angle of the porosity bands according to the definition of Spiegelman (2003) is $\pi/2 - \theta$.

In the modified spherical polar co-ordinate system,

$$\begin{aligned} k_x &= k \cos(\theta) \cos(\psi), \\ k_y &= k \cos(\theta) \sin(\psi), \\ k_z &= k \sin(\theta). \end{aligned}$$

Then eq. (50) becomes

$$\frac{\text{real}(\sigma)}{\sigma_{\text{reaction}}} = \cos^2 \theta + SG(\theta, \psi), \quad (52)$$

where, from eq. (37),

$$G = (\cos^2 \theta \cos^2 \psi - \sin^2 \theta) \cos 2\theta_e + \cos \psi \sin 2\theta \sin 2\theta_e. \quad (53)$$

For the particular case that $\psi = 0$,

$$G = \cos 2(\theta - \theta_e), \quad (54)$$

since the growth rate only depends on the wavevector orientation relative to the direction of extension. Thus $G = 1$ when the wavevector is parallel to the direction of extension and $G = -1$ when they are perpendicular.

Fig. 2 shows the growth rate $\text{real}(\sigma)$ from eq. (52) as a function of θ (x -axis) and ψ (y -axis). This function has four stationary points; we consider each in turn. (i) There is one stationary point at $\theta = \psi = \pi/2$, which is always a saddle point. This is a mode with a wavevector purely in the z -direction. Therefore it represents a tabular perturbation aligned with the x - y plane. (ii) There is another stationary point when $\theta = 0$ and $\psi = \pi/2$. This is a mode with a wavevector purely in the y -direction, that is, geometrically, a tabular feature in the x - z plane. The nature of this stationary point depends on the magnitude of the shear. When S exceeds a critical value $S > S_c \equiv -\cos 2\theta_e$, it is a saddle. However, when $S < S_c$, this stationary point is a maximum. (iii/iv) There are two more stationary points with $\psi = 0$ (so $k_y = 0$) and

$$\tan 2\theta = \frac{2S \sin 2\theta_e}{1 + 2S \cos 2\theta_e}. \quad (55)$$

Fig. 3 shows these modes, which are tabular features that have a wavevector in the x - z plane at an angle θ ; they extend in the y -direction. Eq. (55) has two roots, one in the domain $-\pi/2 \leq \theta < 0$ and another in the domain $0 \leq \theta < \pi/2$. The former root is associated with contractional shear stress and is always a minimum. The latter root is associated with extensional shear stress

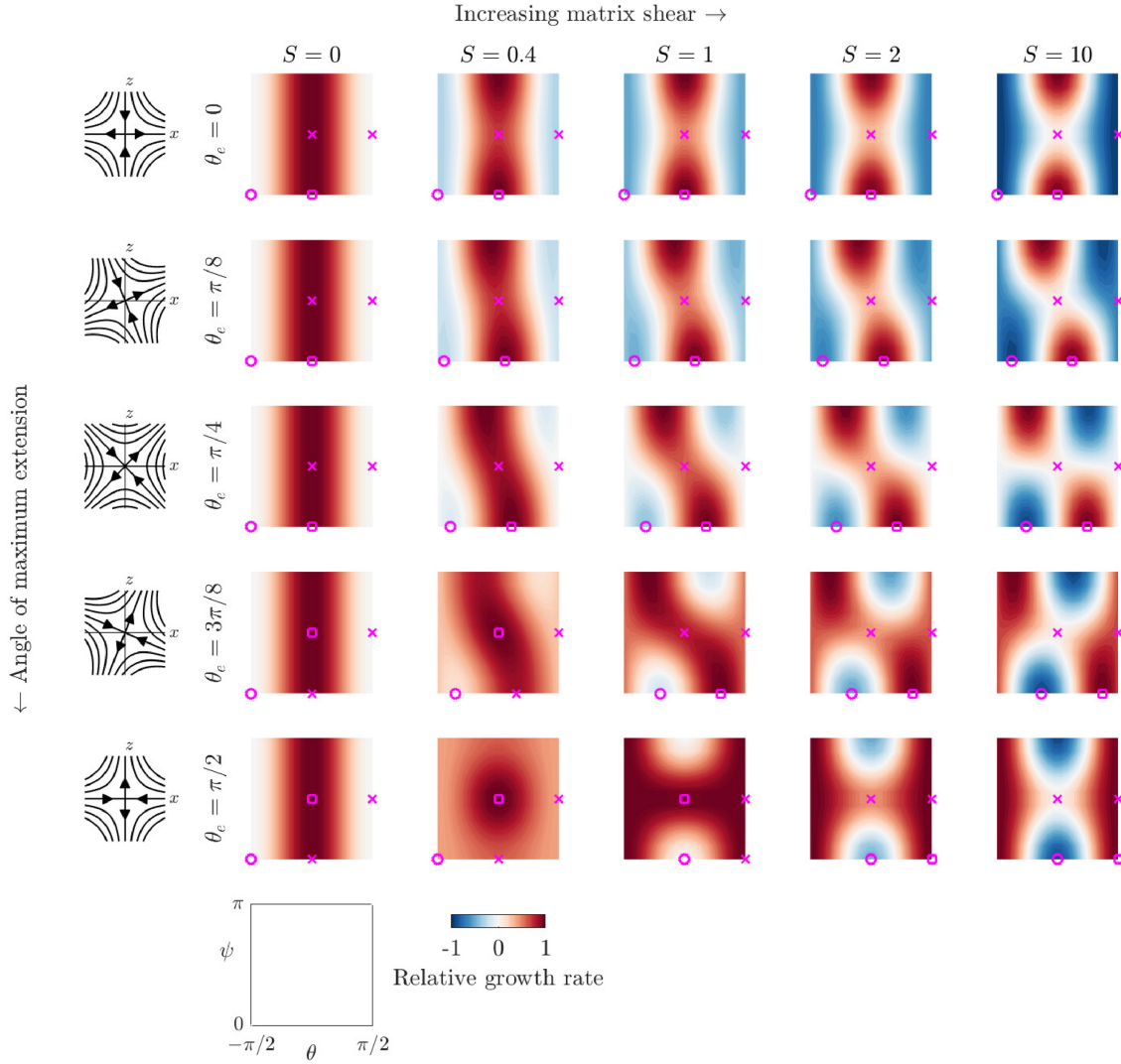


Figure 2. Growth rate from eq. (52) in the range $-\pi/2 < \theta < \pi/2$ (horizontal direction) and $0 < \psi < \pi$ (vertical direction). These axis limits are shown in the labelled diagram on the bottom row. The colour scale shows the normalized growth rate relative to the maximum (growth is red, no growth is white, decay is blue). Crosses represent saddle points, squares represent maxima, circles represent minima. Icons on the left-most column indicate the orientation of the background solid shear flow.

and is a maximum when S exceeds the aforementioned critical value $S > S_c \equiv -\cos 2\theta_e$ and a saddle when $S < S_c$.

We expect the most unstable mode (i.e. the one that grows fastest) to be dominantly expressed in a full solution of the governing equations and hence we analyse what selects this mode. Fig. 4 shows that there is a transition for a horizontally isotropic (no difference between x and y directions) to an anisotropic growth rate as the shear rate S increases, moving from left to right in the figure. However, the transition depends on the angle of maximum extension in the shear flow (from top to bottom in the figure). If $\cos 2\theta_e \geq 0$, which corresponds to the rows with $\theta_e = 0, \pi/8, \pi/4$, the transition is immediately to a state where $k_y = 0$. Geometrically, when $\cos 2\theta_e \geq 0$, the angle of maximum extension is within $\pi/4$ of the horizontal, which means that the horizontal direction is extensional and the vertical direction is contractional, as shown by the mantle flow plots in the left-most column of Fig. 4. This leads to tabular features that are orientated vertically for small S , because reaction dominates the instability and promotes vertical features. The tabular features approach an orientation perpendicular to the angle

of maximum extension as S increases, because this orientation is favoured by the shear-driven instability. However, if $\cos 2\theta_e < 0$, which corresponds to the rows with $\theta_e = 3\pi/8, \pi/2$, the situation is reversed: the x -direction is contractional and the vertical direction is extensional, as shown by the mantle flow plots in the left-most column of Fig. 4. Then for small S , the most unstable wavevector orientation has $k_x = 0, k_z = 0$ (i.e. a tabular feature aligned with the x - z plane) due to the combined effect of reaction and shear. As in previous cases, it is reaction that promotes vertical features ($k_z = 0$). However, in contrast to previous cases, shear-driven contraction suppresses wavevectors in the x -direction so $k_x = 0$. As S increases through the critical value defined above $S_c \equiv -\cos 2\theta_e$ where the shear-driven instability dominates over the reaction-driven instability, the state switches to $k_y = 0$ with orientation approaching the angle of maximum extension for large shear, as before.

MORs, which we will turn to in the second half of the paper, are a horizontally extensional environment, corresponding to the upper rows of Fig. 4. So the crucial implication of this figure for MORs is that even an extremely small shear $S > 0$ is sufficient to break the

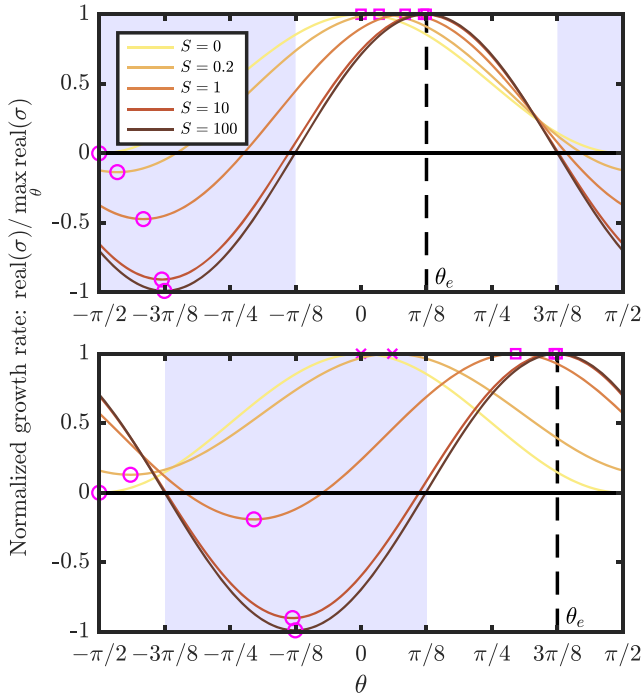


Figure 3. Cross section of the normalized growth rate from Fig. 2 for modes restricted to the x - z plane (i.e. $k_y = 0$) for $\theta_e = \pi/8$ (upper) and $\theta_e = 3\pi/8$ (lower). Note that the normalization is relative to the maximum growth rate for this restricted set of modes, a distinction only relevant where the stationary point is a saddle point (crosses) rather than a maximum (squares).

horizontal isotropy (symmetry under any coordinate rotation about the z -axis) that occurs when only the reactive instability operates. So rather than the expecting the tube-shaped channels that arise from the pure reactive instability ($S = 0$), the most linearly unstable feature with shear $S > 0$ are tabular bands. This is important, because dunite channels (interpreted as relics of high porosity channels) have a tabular morphology, as discussed in Section 1.

3.3 Effect of the compaction length

We now relax the assumption that perturbation wavelength is much shorter than the compaction length. Then eq. (52) generalizes to

$$\frac{\text{real}(\sigma)}{\sigma_{\text{reaction}}} = \frac{1 + k^2 \delta^2 \cos^2 \theta}{1 + k^2 \delta^2} + \frac{SG(\theta, \psi) k^2 \delta^2}{1 + k^2 \delta^2}. \quad (56)$$

This has the same angular dependence as in the small-wavelength limit $k\delta \gg 1$, so all the conclusions of Section 3.2 still hold, including the optimal wavevector orientation.

Fig. 5 shows how the results depend on the compaction length. It shows the normalized growth rate as a function of $k\delta$ for perturbations orientated with $\psi = 0$ and θ chosen to maximize the growth rate. As in Fig. 3, there are two regimes depending on whether the z -direction is in extension or contraction. The upper panel shows the case of $\theta_e = \pi/8$, which has contraction in the z -direction. Here, the contributions to the growth rate from reaction and shear vary oppositely with the compaction length. The reactive contribution, which is the first term on the right-hand-side of eq. (56), decreases slightly with $k\delta$. The amount of decrease depends indirectly on S , because for larger values of S , the angle θ that maximizes the overall growth rate increases from 0 towards θ_e . This decreases $\cos^2 \theta$ in the first term of (56). By contrast, the shear-driven contribution,

which is the second term on the right-hand-side of eq. (56), increases significantly with $k\delta$, starting from zero when $k\delta \ll 1$. Thus the total growth rate is dominated by reaction when $k\delta$ is small, but there can be a cross-over as $k\delta$ increases. This cross-over depends on S . Indeed when S is very small (e.g. the solid curve for $S = 0.2$) reaction always dominates. Physically, the shear-driven instability is suppressed when the wavelength is comparable to the compaction length (Section 2.3), while the reaction-driven instability is not directly affected by compaction in the equilibrium limit ($\tilde{\alpha} = \alpha$). Disequilibrium effects introduce a direct dependence on the compaction length (Rees Jones & Katz 2018).

The lower panel shows the case of $\theta_e = 3\pi/8$, which has contraction in the x -direction. The behaviour is different when $S < S_c = -\cos 2\theta_e$, as illustrated by the solid curves for $S = 0.2$. Unlike the upper panel, the shear-driven contribution decreases with $k\delta$, starting from zero when $k\delta \ll 1$ and decreasing towards a negative value when $k\delta \gg 1$. This is because of the contraction in the direction of the optimal wavevector, consistent with Fig. 3. Thus the total growth rate decreases with compaction length in this case. However, for $S \geq S_c$, there is extension in the direction of the optimal wavevector, and the system behaves in the same way as in the upper panel.

3.4 Disequilibrium effects

So far, we made the assumption that the reaction rate was extremely fast such that $\tilde{\alpha} \approx \alpha$. We now consider the role of disequilibrium effects caused by advective or diffusive chemical transport. We re-write eq. (41)

$$\tilde{\alpha} = \alpha \left[1 + \frac{\phi_0 w_0}{\alpha R \delta} i k \delta \sin(\theta) + \frac{\phi_0 D_X}{\alpha R \delta^2} (k \delta)^2 \right] \quad (57)$$

The two dimensionless parameter groups

$$\text{Da}_w = \frac{\alpha R \delta}{\phi_0 w_0}, \quad \text{Da}_D = \frac{\alpha R \delta^2}{\phi_0 D_X}, \quad (58)$$

are Damköhler numbers that express the reaction rate relative to advective and diffusive transport, respectively. These are typically extremely large and hence the system is typically close to equilibrium (Aharonov *et al.* 1995; Spiegelman *et al.* 2001; Rees Jones & Katz 2018). Physically, advection of undersaturation is negligible when $\text{Da}_w \rightarrow \infty$ and diffusion is negligible when $\text{Da}_D \rightarrow \infty$.

We first restrict attention to the role of advection by taking the limit $\text{Da}_D \rightarrow \infty$ so

$$\tilde{\alpha} = \alpha [1 + i \text{Da}_w^{-1} k \delta \sin(\theta)]. \quad (59)$$

We substitute this expression into eq. (42) and find

$$(1 + \delta^2 k^2) \frac{\text{real}(\sigma)}{\sigma_{\text{reaction}}} = \frac{1 + k^2 \delta^2 \cos^2 \theta}{1 + \text{Da}_w^{-2} (k \delta)^2 \sin^2 \theta} + \frac{S_r G(\theta, \psi) k^2 \delta^2 \sin^2 \theta}{1 + \text{Da}_w^{-2} (k \delta)^2 \sin^2 \theta} + SG(\theta, \psi) k^2 \delta^2, \quad (60)$$

where

$$S_r = S \beta \phi_0 w_0 / \alpha^2 R. \quad (61)$$

We make the approximation $1 + \text{Da}_w^{-2} \sin^2 \theta k^2 \delta^2 \approx 1$ and also take the limit $\delta k \gg 1$. Then eq. (60) simplifies to

$$\frac{\text{real}(\sigma)}{\sigma_{\text{reaction}}} = \cos^2 \theta + SG(\theta, \psi) + S_r G(\theta, \psi) \sin^2 \theta. \quad (62)$$

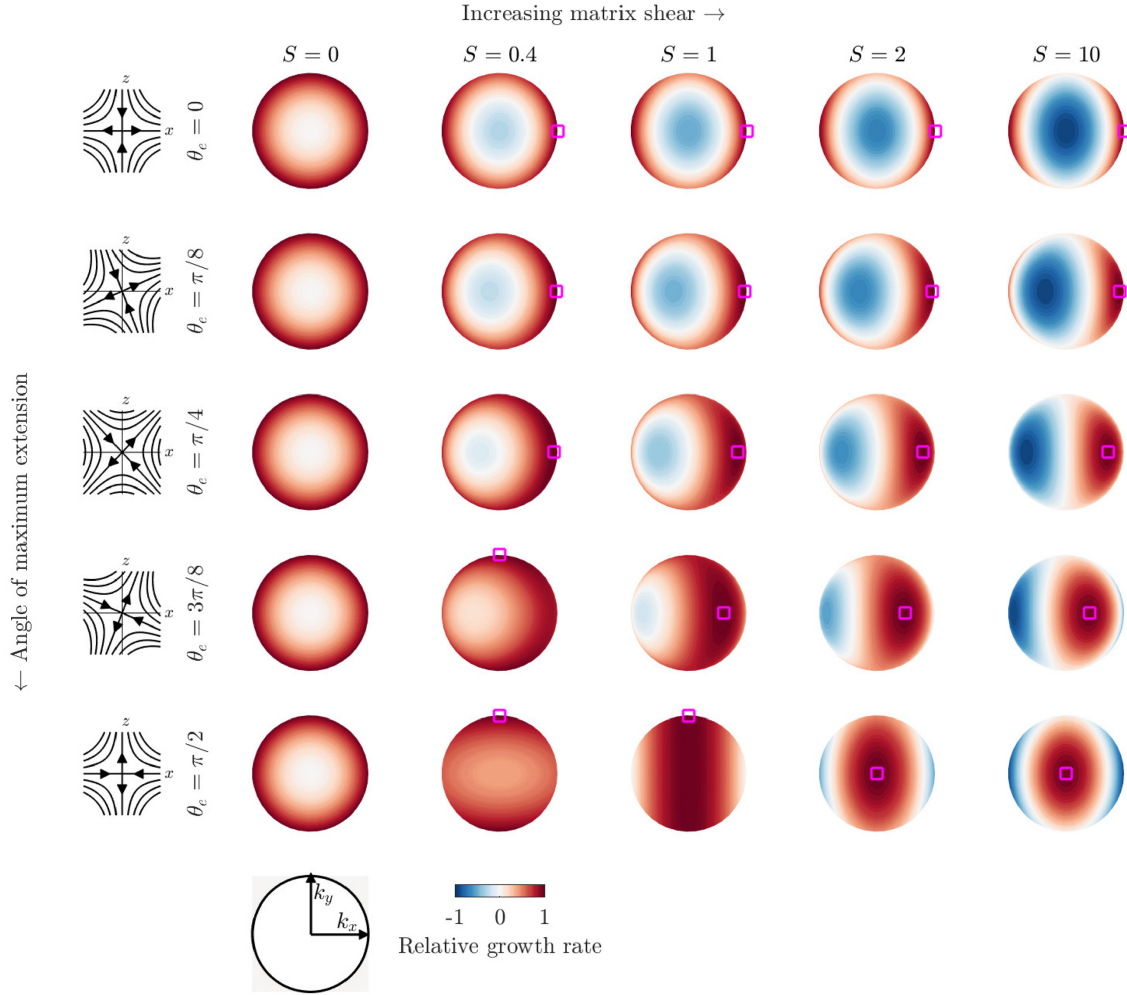


Figure 4. Growth rate from eq. (52) projected on to the k_x – k_y plane, as indicated on the circular icon on the bottom. The growth rate is calculated as a function of (θ, ψ) and then plotted against $[k_x(\theta, \psi), k_y(\theta, \psi)]$. The result is independent of the magnitude of the wavevector. The colour scale shows the normalized growth rate relative to the maximum (red is growth; blue is decay; white is neutral). Squares represent maxima. Squares are not shown for the column $S = 0$; in this case, the maximum growth rate is achieved on the circle $k_x^2 + k_y^2 = k^2$. Icons on the left-most column indicate the orientation of the background solid shear flow.

This expression can be compared to eq. (52) and shows that the advection of undersaturated melts in the presence of shear causes an additional contribution to the growth rate. The contribution is proportional to the shear growth rate, but much smaller, because $\beta\phi_0 w_0/\alpha^2 R \ll 1$, so $S_r \ll S$. Physically, this small contribution comes from the shear-induced perturbation melt flow advecting against the background equilibrium concentration gradient combined with the background melt flow advecting the perturbed undersaturation [see left-hand-side of eq. (19)]. Although this contribution is small, it is physically interesting because it arises from the coupling of the shear and reactive instability, rather than from the sum of their separate rates.

We next turn attention to the role of diffusion by taking the opposite limit $\text{Da}_w \rightarrow \infty$ so

$$\tilde{\alpha} = \alpha [1 + \text{Da}_D^{-1}(k\delta)^2] = \alpha \left[1 + \frac{\phi_0 D_X k^2}{\alpha R} \right]. \quad (63)$$

In the second equality we used $\text{Da}_D^{-1}(k\delta)^2 = \phi_0 D_X k^2/\alpha R$, which depends on the wavelength but is independent of the compaction

length. We substitute this expression into eq. (42) and find

$$(1 + \delta^2 k^2) \frac{\text{real}(\sigma)}{\sigma_{\text{reaction}}} = \frac{1 + k^2 \delta^2 \cos^2 \theta}{1 + (\phi_0 D_X/\alpha R)k^2} + SG(\theta, \psi)k^2 \delta^2, \quad (64)$$

Again, in the limit $\delta k \gg 1$, eq. (64) simplifies to

$$\frac{\text{real}(\sigma)}{\sigma_{\text{reaction}}} = \frac{\cos^2 \theta}{1 + (\phi_0 D_X/\alpha R)k^2} + SG(\theta, \psi). \quad (65)$$

In this case there is no new contribution to the growth rate; the only change is that the reactive contribution to growth is slightly reduced, especially at high wavenumber (because diffusion acts at small length scales), as discussed in Rees Jones & Katz (2018).

In the next section we embed the above considerations of perturbation growth into the background, large-scale flow beneath a MOR. We neglect both disequilibrium effects and also the role of compaction length (equivalently, the role of the wavenumber). Fig. 5 indicates that the growth rate depends weakly on wavenumber provided $(k\delta)^2 \gtrsim 100$, or equivalently provided the wavelength is less than about $\delta \times 10/2\pi \approx 1.6$ km, for a compaction length $\delta \approx 1$ km. Given that observed dunite channels are smaller than this (Braun & Kelemen 2002), we make the simplifying assumption that $k\delta \gg 1$.

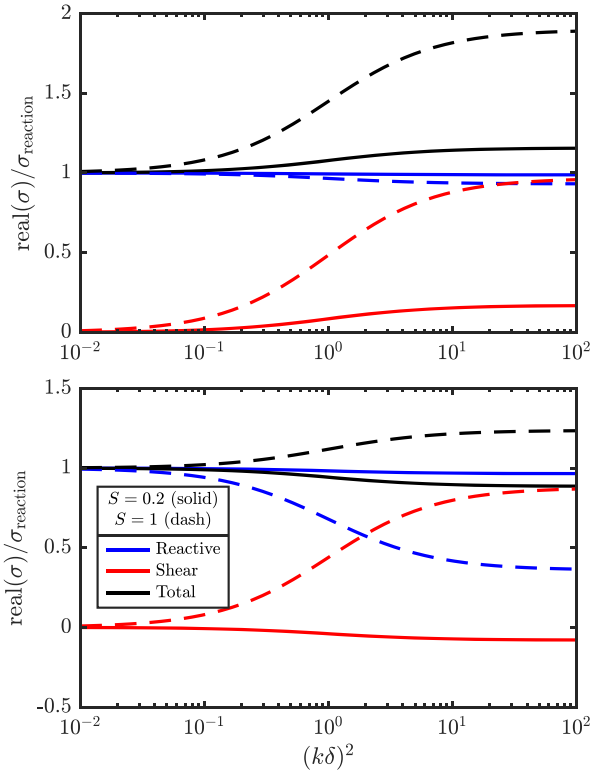


Figure 5. Dependence on normalized compaction length $k\delta$. As in Fig. 3, the upper panel shows $\theta_e = \pi/8$ and the lower panel shows $\theta_e = 3\pi/8$. In both panels, we plot eq. (56) for $\psi = 0$ and θ chosen to maximize the growth rate according to eq. (55).

4 METHODS: GROWTH OF INSTABILITIES AT MORs

At MORs, plate spreading drives a circulation of the upper mantle. This is a viscous shear flow and so could promote the formation of shear-driven porosity bands. The upwelling of the mantle beneath the ridge causes decompression melting in a roughly triangular region down to a depth of around 80 km (Langmuir *et al.* 1992). The resulting melt upwells due to its buoyancy. Over this depth (and hence pressure) range, there is a gradient in the equilibrium chemistry of magma that can drive reactive melting (Kelemen *et al.* 1992, 1995a; Longhi 2002). Thus MORs are a geological setting where both shear-driven and reaction-driven porosity localization have the potential to occur. In this section, we estimate the relative and combined contributions of these mechanisms. We discuss the predicted orientation of the localized features that result from perturbation growth.

4.1 Background state of the MOR

Our approach combines models of several aspects of MORs with the calculations of the growth rate of porosity bands made above. First we estimate the background state, that is, the behaviour of the system in the absence of any small-scale localization of porosity. Our estimates focus on the partially molten region beneath the lithosphere, shown in Fig. 6. For present purposes, the lithosphere is defined as a rigid plate, moving uniformly away from the ridge axis at a speed U_0 . In Section 4.1.1, we calculate the passive flow of the partially molten mantle as the response to motion of the lithosphere. In

Section 4.1.2, we calculate the background magma flow and porosity by dividing the partially molten region into a series of melting columns in which magma rises vertically. We assume that each of these melting columns terminates at the base of the lithosphere. This simple formulation for the background-state magma flow precludes capture of lateral flows associated with gradients in compaction pressure (e.g. melting-rate-pressure focusing (Turner *et al.* 2017; Sim *et al.* 2020)), focusing within a decompression channel immediately beneath the lithosphere (Sparks & Parmentier 1991; Spiegelman 1993; Ghods & Arkani-Hamed 2000). However, if melt transport throughout most of the melting region (aside from a narrow region near the base of the lithosphere) is buoyancy-driven and hence nearly vertical, our representation is valid, if approximate. We return to this issue in Section 6.3.

4.1.1 Mantle flow and strain rate

We estimate the background flow by treating the mantle as a uniform, isoviscous material that flows in response to prescribed plate motion. This is sometimes called a passive or kinematic model. In treating the mantle as isoviscous, we are neglecting the variation of shear viscosity with the background porosity. Based on the parameters estimated subsequently ($\lambda^* = 26$, $\phi_0 \lesssim 2 \times 10^{-3}$), this is a reasonable approximation since $e^{-26 \times 2 \times 10^{-3}} \approx 0.95$, that is, only about a 5 per cent reduction in viscosity. Equations governing the flow of an isoviscous material in a triangular region are given by Batchelor (1967) and applied to a MOR melting region by Spiegelman & McKenzie (1987). Here, we summarize these results.

Fig. 6(a) shows the co-ordinate system, centred on the ridge axis, with x the horizontal distance from the ridge and z the vertical distance from the surface, measured upwards, such that $z = -H$ is the bottom of the melting region. The corner-flow solution is most naturally expressed in polar co-ordinates (r, ϑ) , where r is the distance to the origin and ϑ is the angle to the downward vertical (so $\vartheta = 0$ is straight down). The partially molten region is triangular and extends to $\vartheta = \pm\vartheta_1$, where $\pi/2 - \vartheta_1$ is the dip of the bottom of the lithosphere.

There is a separable solution in this geometry where the radial flow u_r and tangential flow u_ϑ can be written

$$u_r = -U_0 \Theta'(\vartheta), \quad u_\vartheta = U_0 \Theta(\vartheta). \quad (66)$$

The function $\Theta(\vartheta)$ that satisfies the relevant boundary conditions (that the flow is symmetric about the ridge axis and uniformly translating at speed U_0 in the lithosphere) is

$$\Theta(\vartheta) = \frac{\vartheta \cos \vartheta - \sin \vartheta \cos^2 \vartheta_1}{C}, \quad (67)$$

where $C = \vartheta_1 - \sin \vartheta_1 \cos \vartheta_1$ is a constant that depends only on the geometry of the melting region.

We can convert from polar to scaled Cartesian co-ordinates $\tilde{z} = -\tilde{r} \cos \vartheta$, $\tilde{x} = \tilde{r} \sin \vartheta$, where all distances are scaled by H , for example, $\tilde{r} = r/H$. Then the scaled solid velocity $\tilde{\mathbf{u}} = \mathbf{u}/U_0$ has components

$$\tilde{u}_x = \frac{\tilde{x}\tilde{z}/\tilde{r}^2 - \arctan(\tilde{x}/\tilde{z})}{C}, \quad \tilde{u}_z = \frac{\tilde{z}^2/\tilde{r}^2 - \cos^2 \vartheta_1}{C}. \quad (68)$$

The scaled velocity gradient tensor is

$$\tilde{\nabla} \tilde{\mathbf{u}} = \frac{1}{C\tilde{r}^4} \begin{bmatrix} -2\tilde{x}\tilde{z}^2 & 0 & 2\tilde{x}^3 \\ 0 & 0 & 0 \\ -2\tilde{x}\tilde{z}^2 & 0 & 2\tilde{x}\tilde{z}^2 \end{bmatrix}, \quad (69)$$

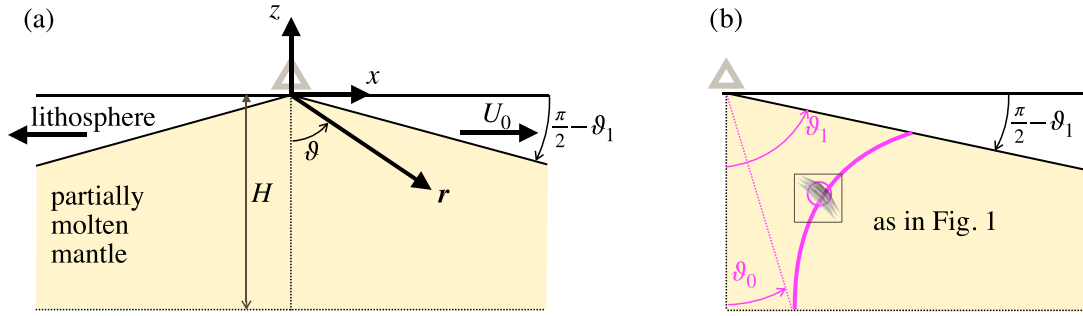


Figure 6. Sketch of mid-ocean ridge model, which is symmetric about the ridge axis. (a) Coordinate system for the mid-ocean ridge model where the base of the lithosphere makes an angle $\pi/2 - \theta_1$ from the horizontal. The lithosphere spreads rigidly at a speed U_0 away from the ridge axis. The grey triangle represents the mid-ocean ridge axial volcano. This ‘corner-flow’ geometry is taken from Spiegelman & McKenzie (1987). Our model is concerned with the partially molten mantle, which is shaded yellow. (b) The magenta curve shows a streamline of the solid mantle corner flow, which starts from the base of the melting region at angular position θ_0 and finishes at θ_1 . We evolve a parcel of porosity bands along the streamline.

which has a symmetric part

$$\tilde{\mathbf{D}} = \frac{1}{C\tilde{r}^4} \begin{bmatrix} -2\tilde{z}\tilde{x}^2 & 0 & \tilde{x}(\tilde{x}^2 - \tilde{z}^2) \\ 0 & 0 & 0 \\ \tilde{x}(\tilde{x}^2 - \tilde{z}^2) & 0 & 2\tilde{z}\tilde{x}^2 \end{bmatrix}. \quad (70)$$

Then, by comparison with eq. (27), we find that the dimensional strain rate is

$$\dot{\gamma} = \frac{U_0}{H} \frac{1}{C} \frac{|\tilde{x}|}{\tilde{r}^2} = \frac{U_0}{H} \frac{1}{C} \frac{|\sin \vartheta|}{\tilde{r}}, \quad (71)$$

and the direction of maximum extension is

$$\theta_e = \vartheta - \frac{\pi}{4} \text{sign}(\vartheta). \quad (72)$$

Thus when $x < -z$, the angle of maximum extension is below the horizontal ($\theta_e < 0$) and vice versa when $x > -z$. The strain rate is zero beneath the ridge axis ($x = 0$) and increases in approach to the base of the lithosphere (as x increases or r decreases). The term involving $\text{sign}(\vartheta)$ in eq. (72) arises because $\dot{\gamma} > 0$ by definition, leading to the the modulus operator in eq. (71). In cylindrical polar co-ordinates, the only non-zero components of the symmetric rate-of-strain tensor are $D_{r\vartheta} = D_{\vartheta r} = \dot{\gamma}$ [which can be seen from the separable solution in terms of $\Theta(\vartheta)$]. Fig. 7(a) shows this background strain rate.

The other information that we need for the magma flow calculations in the following section is the mantle upwelling speed W_b at the base of the melting column (where $\tilde{z} = -1$ and $\tilde{r}^2 = 1 + \tilde{x}^2$). Here,

$$W_b = U_0 \frac{(1 + \tilde{x}^2)^{-1} - \cos^2 \vartheta_1}{C}. \quad (73)$$

As expected, this equation says that the upwelling speed decreases with distance from the ridge axis.

4.1.2 Magma flow and porosity

We estimate the background magma flow and porosity by dividing the melting region into a series of 1-D melting columns. The methodology for calculating the flow in a melting column was originally devised by Ribe (1985). The presentation and notation is based on Rees Jones & Rudge (2020), which develops a revised estimate of magma velocities based on the magmatic response to the deglaciation of Iceland (MacLennan *et al.* 2002).

We start from the equations of two-phase flow presented in Section 2.1. Making the same simplifications and taking the special

case of a 1-D flow at steady state, eqs (15) and (16) imply that

$$\frac{d}{dz}(\phi w) = \Gamma, \quad (74)$$

where w is the vertical component of the magma velocity. Then we take $\Gamma = \Gamma_0$, where Γ_0 is the rate of decompression melting, which we assume to be uniform within the melting column. This is a reasonable approximation in the present context, but it neglects the drop in productivity when a mineral phase is exhausted from the residue (Hirschmann *et al.* 1999). Moreover, it does not apply for volatile-driven melting at depths beneath the dry (i.e. volatile-free) solidus, or at the transition to dry melting (Keller & Katz 2016).

As an aside, note that in our earlier development of the method in Section 2 we could have used an alternative melting-rate parametrization. In place of eq. (19), we could have used

$$\Gamma = \Gamma_0 + \frac{\beta}{\alpha} \phi \mathbf{v}_l \cdot \tilde{\mathbf{z}}, \quad (75)$$

in which case Γ_0 would have entered the base state calculations but would not have affected the linear equations governing the perturbations. The most important difference is that the background compaction rate would no longer have been negligible, which would have complicated the analysis. Physically, the background compaction rate is a stabilizing influence on the reaction-infiltration instability, the magnitude of which is very sensitive to the dependence of bulk viscosity on porosity (Hewitt 2010; Rees Jones & Katz 2018). The parametrization of eq. (75) also neglects the disequilibrium effects (Section 3.4). Thus we use eq. (19) to calculate the melting rate throughout this study, which maintains consistency with previous studies of the reaction-infiltration instability (Aharonov *et al.* 1995; Rees Jones & Katz 2018).

Eq. (74) can be integrated, with the constant of integration chosen such that $\phi w = 0$ at the base of the melting column $z = -H$,

$$\phi w = \Gamma_0(z + H) = F_{\max} W_b(1 + \tilde{z}), \quad (76)$$

in which we made use of the fact that $\Gamma_0 H = F_{\max} W_b$, where F_{\max} is the maximum degree of melting and W_b is the mantle upwelling velocity at the base of the column.

Then we take eq. (18) and assume that background magmatic segregation is entirely driven by buoyancy to obtain

$$\phi w = Q_0 \phi^n, \quad Q_0 = K^* \Delta \rho g, \quad (77)$$

where K^* is the prefactor in the permeability–porosity relationship $K = K^* \phi^n$, and $\Delta \rho g$ is the buoyancy associated with the density

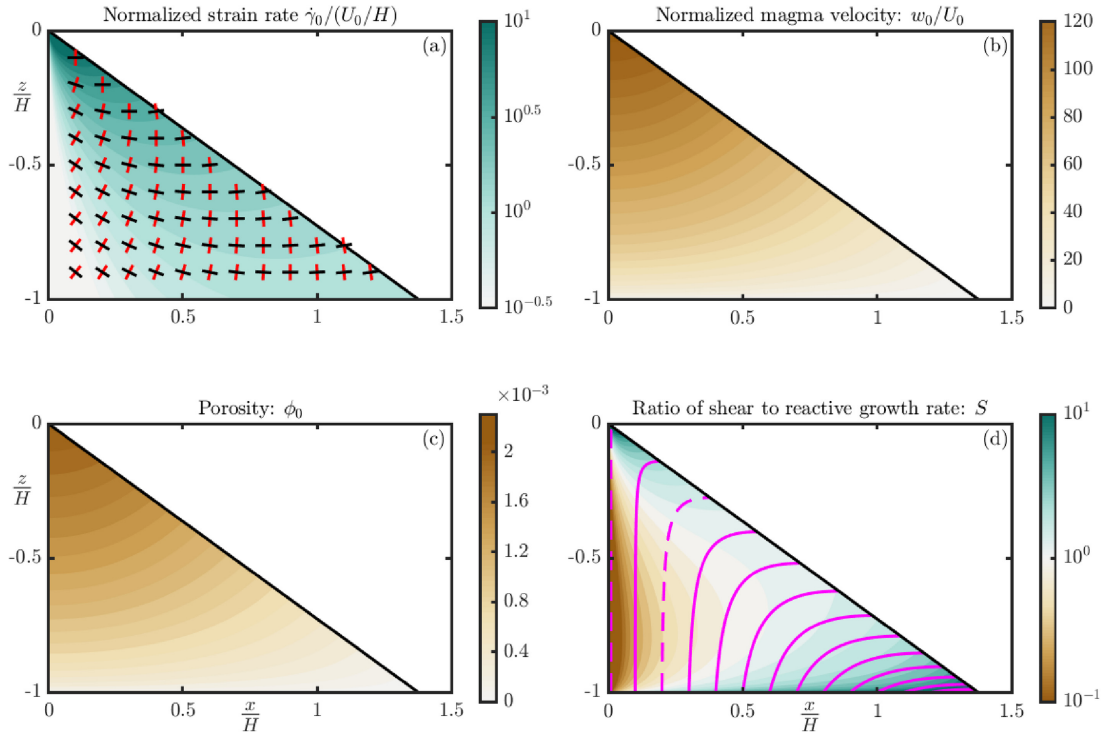


Figure 7. Background state of a mid-ocean ridge. (a) Strain rate with black/red markers showing the direction of extension/contraction, respectively; (b) magma velocity; (c) porosity. Note that the maximum porosity is about 2×10^{-3} , which is equivalent to 0.2 per cent. (d) Ratio of local growth rate due to shear versus reaction. Brown colours indicate where reactive instability is favoured. Green colours indicate where shear is favoured. Magenta curves show streamlines of the solid flow, along which the growth of the instability is integrated (Section 4.2.2). Two streamlines are dashed—these are used as examples in Fig. 11. The parameters used are discussed in Section 4.1.3.

difference between solid and liquid phases (see Section 2.2). We combine eqs (76) and (77) to obtain

$$\phi = [F_{\max} W_b (1 + \tilde{z})]^{\frac{1}{n}} Q_0^{-\frac{1}{n}}, \quad (78)$$

$$w = [F_{\max} W_b (1 + \tilde{z})]^{\frac{n-1}{n}} Q_0^{\frac{1}{n}}. \quad (79)$$

We combine this last expression with eq. (73) to obtain an expression for the background rate of magmatic upwelling relative to the plate half-spreading rate,

$$\frac{w_0}{U_0} = \left[\frac{F_{\max}}{C} ((1 + \tilde{x}^2)^{-1} - \cos^2 \vartheta_1) \right]^{\frac{n-1}{n}} \times [1 + \tilde{z}]^{\frac{n-1}{n}} [Q_0/U_0]^{\frac{1}{n}}. \quad (80)$$

Here, we relabelled w as w_0 , using a subscript to refer to a background property, consistent with the convention introduced in Section 2.2. Fig. 7(b) plots the ratio w_0/U_0 , and Fig. 7(c) shows the corresponding background porosity, denoted ϕ_0 . These plots are sensitive to the efficiency of melt extraction Q_0 . If melt extraction is more efficient (Q_0 is higher), then the relative melt velocity w_0/U_0 is increased, reflecting the proportionality to $Q_0^{1/n}$ in eq. (80). The steady-state porosity ϕ_0 is a balance between melt production and melt extraction. Thus if melt extraction is more efficient (Q_0 is higher), then ϕ_0 is decreased, reflecting the proportionality to $Q_0^{-1/n}$ in eq. (78).

4.1.3 Choice of parameters

Our calculations use a reference set of parameters to illustrate the typical behaviour of the model. This includes a prescribed dip of the base of the lithosphere of $\pi/5$ (36°), as an intermediate case between a very steep boundary ($\pi/4$, or 45°) and a much shallower case. Later, in Section 5.4, we consider the behaviour when $\pi/12$ (15°), which might be appropriate if the lithosphere is interpreted to be the cold thermal boundary, which thickens gradually at intermediate to fast spreading rates.

Reference material parameters are estimated from laboratory experiments and micromechanical models. We use a porosity–permeability exponent $n = 2$, appropriate for small porosity as found in Fig. 7(c), from the micromechanical model of Rudge (2018). At larger porosity, the exponent may be higher according to laboratory experiments (e.g. Wark & Watson 1998; Connolly *et al.* 2009; Miller *et al.* 2014). The sensitivity of shear viscosity to porosity was estimated experimentally to be $\lambda^* = 26$ by Mei *et al.* (2002). Micromechanical models (Takei & Holtzman 2009a; Rudge 2018) indicate that this factor decreases with increasing porosity, but is similar to the estimate $\lambda^* = 26$ when porosity is fairly small [see, e.g. fig. 13 of Rudge (2018)]. The bulk-to-shear viscosity ratio has been extensively debated and has not been directly measured experimentally. Micromechanical models offer different predictions depending on assumptions about the microphysics of creep. There are two main categories. Models that assume viscous deformation at the microscale have bulk viscosity proportional to η/ϕ , so the bulk-to-shear viscosity ratio is very large [$O(10^2)$, for example Simpson *et al.* 2010]. Models that assume diffusion at the microscale (either

volumetric or grain boundary diffusion) have a much weaker sensitivity to porosity and the bulk-to-shear viscosity ratio is moderate [$O(1)$, e.g. Takei 1998; Rudge 2018]. We take the estimate $\zeta_0/\eta_0 = 5/3$ as our reference case and consider the possibility that the ratio is much higher in Section 5.4.

The melt velocity depends on the maximum degree of melting, for which we take $F_{\max} = 0.2$ as a typical value. It also depends on the ratio Q_0/U_0 . As a reference value we take $Q_0/U_0 = 6.3 \times 10^4$, which for $U_0 = 3 \text{ cm yr}^{-1}$ corresponds to a maximum melt velocity of 4 m yr^{-1} . Q_0 is sensitive to the reference permeability of the mantle, which is poorly constrained. Rees Jones & Rudge (2020) argue that the maximum melt velocity is faster than this. Here we make a relatively conservative choice such that in our reference case, both reaction and shear have the potential to make similar contributions to the growth of porosity bands. We consider faster and slower melt segregation in Section 5.4. The overall amount of reactive melts generated depends on the parameter group $\beta H/\alpha \approx 0.2$ (probably within a range 0.15–0.3), based on previous studies of the reaction-infiltration instability (Aharonov *et al.* 1995; Rees Jones & Katz 2018).

4.2 Combined instability at MORs

We now use reference parameters to combine this MOR background state with the calculation of the linear growth rate. We estimate the growth of instabilities caused by reaction and shear. Fig. 6(b) illustrates our approach, which is based on evolving a local parcel of porosity bands along each streamline of the solid mantle flow, as we now describe in detail.

4.2.1 The role of porosity advection

Our previous calculations in Section 3 concerned the growth rate of instability in an infinite, uniform medium. For a MOR however, we must consider how to treat the advection of porosity in eq. (5). We write that equation as

$$\frac{\partial \phi}{\partial t} + \mathbf{v}_s \cdot \nabla \phi = f, \quad (81)$$

where f is a general source term representing the effect of compaction and reaction. This equation contains the only time derivative and the only solid-velocity advection term in the overall set of equations and its treatment has been considered by previous studies. Spiegelman (2003) showed that the rotational part of a linear flow causes an evolution in the angle of porosity bands. For simple shear, $\mathbf{v}_s \propto [z, 0, 0]$, Spiegelman (2003) used a generalized linear analysis where the wavevector depends on time such that $\phi' \propto \exp(i \mathbf{k}(t) \cdot \mathbf{x})$. Butler (2010) showed that both a pure and also a simple shear flow cause the wavelength of porosity bands to increase. Gebhardt & Butler (2016) extended the methodology of Spiegelman (2003) to a general flow with translation and shear, and applied it to the solid velocity field of a MOR setting.

In this section, we use the same approach as Gebhardt & Butler (2016). The only new aspect of our calculation involves the growth rate σ , where we account for growth of instabilities by reactive infiltration as well as shear. We now give a slightly expanded justification for the methodology. We introduce a local co-ordinate system about some arbitrary point \mathbf{x}_0 and let \mathbf{x} be the (small) displacement from that point. We then Taylor expand the solid velocity to first order about the point using the velocity gradient tensor

$$\mathbf{v}_s(\mathbf{x}_0 + \mathbf{x}) \approx \mathbf{v}_0 + \nabla \mathbf{v}_s \cdot \mathbf{x}, \quad \mathbf{v}_0 = \mathbf{v}_s(\mathbf{x}_0), \quad (82)$$

where the velocity gradient tensor $\nabla \mathbf{v}_s$ is evaluated at \mathbf{x}_0 . Thus the velocity gradient tensor in the approximation is locally a constant, so the corresponding term $\nabla \mathbf{v}_s \cdot \mathbf{x}$ is a linear shear flow of the type discussed in Section 2. We express the porosity as a generalized normal mode:

$$\phi = \phi_0 + \exp[i \mathbf{k}(t) \cdot \mathbf{x} + s(t)], \quad (83)$$

where ϕ_0 is the background state and $\mathbf{k}(t)$ is the wavevector of a disturbance and $s(t)$ determines its amplitude. The wavevector and amplitude evolve according to

$$\frac{D\mathbf{k}}{Dt} + \nabla \mathbf{v}_s^T \cdot \mathbf{k} = 0, \quad (84)$$

$$\frac{Ds}{Dt} = \sigma, \quad (85)$$

where $\frac{D}{Dt} \equiv \frac{\partial}{\partial t} + \mathbf{v}_0 \cdot \nabla$ is the Lagrangian derivative (or equivalently the derivative along a streamline of the solid flow). These equations are sufficient to ensure that the porosity advection eq. (81) is satisfied, provided $f \approx f_0 + \sigma(\phi - \phi_0)$, where f_0 is the background part of the source term. This can be verified by substituting eq. (83) into eq. (81) with the velocity expanded using eq. (82). The terms involving the uniform translation \mathbf{v}_0 are accounted for by the switch to the Lagrangian derivative. The terms involving the wavevector can be shown to cancel by taking the scalar (dot) product of eq. (84) with the vector \mathbf{x} .

This approach to evolution of porosity perturbations is local, and is only valid when the solid velocity varies on some scale very much larger than the wavelength of the perturbation. It can be made precise in certain situations, including that of Spiegelman (2003), which considers a uniform background state and a linear shear flow. However, as Gebhardt & Butler (2016) discuss, for MORs it should be thought of as a reasonable, if *ad hoc*, estimate of the behaviour of porosity bands. This is because the calculation of σ was for an infinite domain with a uniform background porosity, uniform magma flow field and linear mantle shear flow. These will all be reasonable approximations provided the wavelength of the porosity bands is small, in which case the bands vary on scale much shorter than that over which the background porosity evolves, and so the growth rate calculation should be reasonably accurate.

4.2.2 Integration along streamlines

We now integrate eqs (84) and (85) along streamlines of the solid flow, as shown in Figs 6(b) and 7(d). It is possible to do this in Cartesian co-ordinates, but preferable to work in polar co-ordinates because the equation of a streamline is particularly simple. Consider a streamline $(\tilde{r}(t), \vartheta(t))$ that starts at $(\tilde{r}_0, \vartheta_0)$ when $t = 0$. By choosing $\tilde{r}_0 = 1/\cos \vartheta_0$, all the streamlines start at the base of the melting region. Then a streamline is defined by

$$\tilde{r}\Theta(\vartheta) = \text{constant} \Rightarrow \tilde{r}(\vartheta) = \frac{\Theta(\vartheta_0)}{\cos \vartheta_0} \frac{1}{\Theta(\vartheta)}. \quad (86)$$

Thus given ϑ , we have an explicit expression for \tilde{r} and hence (\tilde{x}, \tilde{z}) along the streamline, if required. Then we have an evolution equation for ϑ , namely

$$\frac{d\vartheta}{dt} = \frac{u_\vartheta}{r} = \frac{U_0}{H} \frac{\Theta(\vartheta)}{\tilde{r}(\vartheta)}. \quad (87)$$

Since we are integrating along streamlines, the material derivatives D/Dt can be replaced by full derivatives d/dt . Finally, we can change variables to make ϑ the independent variable instead of t using eq. (87). Thus

$$\frac{d\mathbf{k}}{d\vartheta} = -\frac{\tilde{r}(\vartheta)}{\Theta(\vartheta)} \tilde{\nabla} \tilde{\mathbf{u}}^T \cdot \mathbf{k}, \quad (88)$$

$$\frac{ds}{d\vartheta} = \frac{\tilde{r}(\vartheta)}{\Theta(\vartheta)} \frac{H\sigma}{U_0}. \quad (89)$$

This system of equations can be integrated over the range of $\vartheta_0 \leq \vartheta \leq \vartheta_1$ using any standard ODE solver (we use the MATLAB routine ODE45). This procedure is repeated for a range of initial positions specified by ϑ_0 . The system is linear in the initial amplitude so we take $s = 0$ as an initial condition. We also need to specify an initial condition on the wavevector (see Section 4.2.4). Note that the change of variables to ϑ breaks down exactly beneath the ridge axis (by construction, since ϑ is not varying along that streamline). For that special case, it is easiest to use z as the independent variable.

4.2.3 Overall growth rate

The amplitude of the instability evolves along a streamline according to eq. (89). We neglect the imaginary part of the growth rate (which gives rise to transient waves) and use the simplest expression for the real part of the growth rate (52), in which the contributions from reaction and shear can be computed separately. Thus we split the amplitude s from eq. (83) into a part arising from reaction s_{reaction} and a part arising from shear s_{shear} .

For reaction-driven instabilities, we find

$$\frac{d}{d\vartheta} s_{\text{reaction}} = n \frac{\beta H}{\alpha} \frac{w_0}{U_0} \frac{\tilde{r}(\vartheta)}{\Theta(\vartheta)} \cos^2 \theta. \quad (90)$$

Thus the magnitude of the reactive growth rate depends on the following dimensionless parameters: the permeability exponent $n = 2$, the overall amount of reactive melts generated $\beta H/\alpha = 0.2$, and the relative magma velocity w_0/U_0 given by eq. (80). This latter ratio can be significantly greater than 1, allowing the contribution from the reactive instability to be significant.

For shear-driven instabilities, we find

$$\frac{d}{d\vartheta} s_{\text{shear}} = \frac{2\lambda^*}{\frac{4}{3} + \frac{\xi_0}{\eta_0}} \frac{|\sin \vartheta|}{C\Theta(\vartheta)} G(\theta, \psi), \quad (91)$$

in which we used eq. (71). Crucially, this is independent of the plate half-spreading rate. Although a faster spreading rate increases the strain rate, which increases σ_{shear} , it also increases the solid mantle velocity, thereby reducing the time spent to move through the partially molten region (proportional to H/U_0). Instead, the shear-driven instability depends only on a combination of rheological properties $2\lambda^*/\left(\frac{4}{3} + \frac{\xi_0}{\eta_0}\right)$, relative position in space (via ϑ and ϑ_1), and orientation of the wavevector.

4.2.4 Initial conditions and evolution of the wavevector

We specify the wavevector at the start of a streamline as an initial condition. The wavevector then evolves according to eq. (88), where $\tilde{\nabla} \tilde{\mathbf{u}}$, obtained from the corner flow, is given by eq. (69). We choose an initial condition $k_y = 0$. Then by eq. (88), k_y remains zero. This choice of initial condition is motivated by the fact that a MOR has extension in the horizontal, which favours a wavevector orientation with $k_y = 0$, as discussed in Section 3.2.

We take two approaches to specify the initial condition. First, we prescribe a single initial orientation of the wavevector. Secondly, we prescribe a uniform distribution of wavevector orientation, an approach also taken by Gebhardt & Butler (2016).

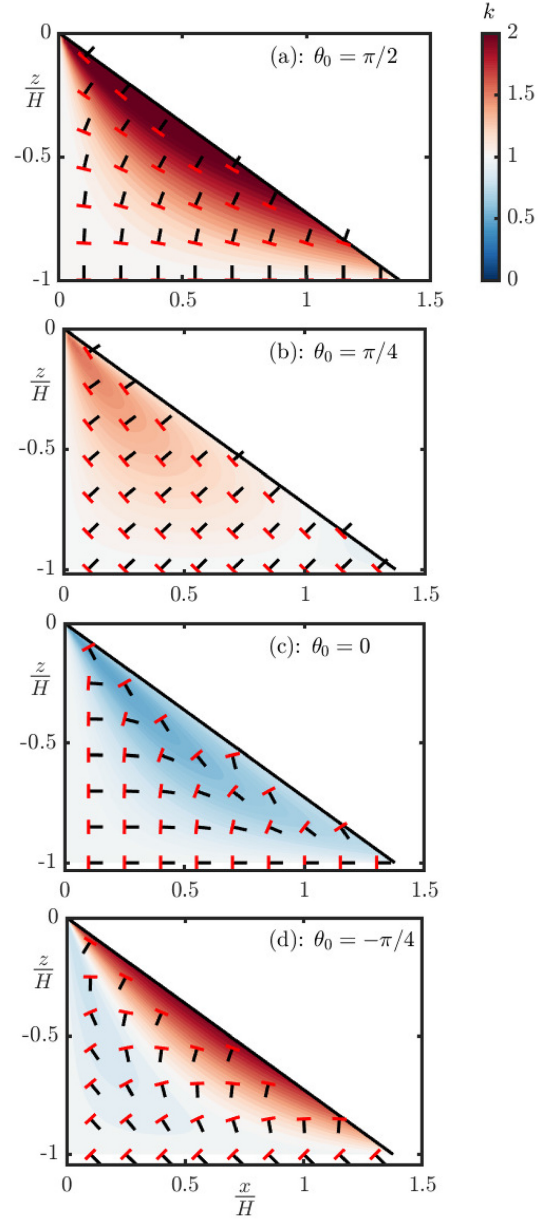


Figure 8. Effect of shear on orientation and magnitude of wavevector. In each panel, the initial magnitude of the wavevector is 1 and the initial orientation is: (a) $\theta_0 = \pi/2$, (b) $\theta_0 = \pi/4$, (c) $\theta_0 = 0$ and (d) $\theta_0 = -\pi/4$. Black line segments show the orientation of the wavevector and red line segments show the corresponding porosity bands, which are perpendicular to the wavevector. The colourscale shows the wavenumber, with red colours corresponding to increased wavenumber (reduced wavelength) and blue colours corresponding to reduced wavenumber (increased wavelength).

Fig. 8 shows the effect of the corner flow on the wavevector, starting from a single initial orientation. The flow acts to rotate the wavevector in a clockwise sense to the right of the ridge axis (decreasing θ). The wavenumber variation depends on whether the flow resolved along it is extensional or contractional. However, the maximum change of wavenumber (and hence of wavelength) is a factor of about 2 of its initial value. Given that the growth rate is only weakly sensitive to wavelength (assuming it is smaller than the compaction length), we can infer that the effect of solid flow on the wavenumber is mainly through rotation.

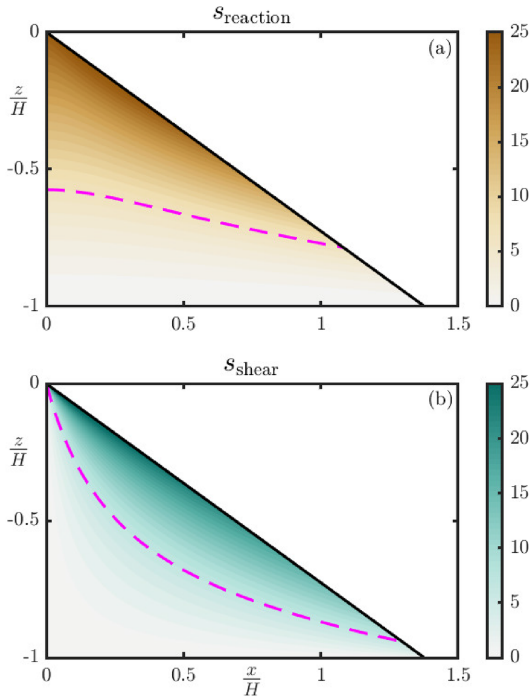


Figure 9. Total growth of (a) reactive and (b) shear-driven instabilities. The dashed magenta curve highlights the contour $s = 7$, which corresponds to an increase in amplitude of about 10^3 .

5 RESULTS: GROWTH OF INSTABILITIES AT MORs

Results are described in the following order. First, in Section 5.1, we calculate the maximum possible growth of the instability by assuming that the wavevector is always instantaneously in the optimal orientation. Second, in Section 5.2, we calculate the growth for a prescribed initial wavevector orientation that evolves along streamlines. Third, in Section 5.3, we calculate the growth for a distribution of initial wavevector orientations. Finally, in Section 5.4, we discuss how the results depend on the choice of parameters.

5.1 Orientation-independent, maximal growth

To facilitate an understanding of instability growth in the context of our MOR background state, we first present results where growth rates are maximized over all possible perturbation orientations θ . In particular, for reaction we take $\cos^2 \theta = 1$ in eq. (90), and for shear we take $G(\theta, \psi) = 1$ in eq. (91). This approach gives an upper bound on growth, because the factors involving the wavevector orientation are always less than or equal to 1 in magnitude.

Fig. 7(d) compares the ratio of local maximum growth rate due to shear versus that due to reaction. Reaction is dominant beneath the ridge axis and shear is dominant off-axis along the base of the lithosphere. This reflects the pattern of background strain rate (which is zero on the axis) and magma segregation speed (which decreases away from the axis), as shown in other panels of Fig. 7.

Fig. 9 shows the maximum possible accumulated growth of perturbations. The maximum possible growth is comparable between the two mechanisms, but this is sensitive to the choice of parameters. If the magma velocity were assumed faster or the ratio of bulk to shear viscosity were higher, the reactive growth would be much larger than the shear-driven growth (see Section 5.4 for a fuller sensitivity analysis). Even the reference parameter choices (that allow

both reaction and shear to contribute) emphasize an important result: beneath the ridge axis, reaction dominates in the formation of channels. The dashed magenta contours in Fig. 9 highlight where the amplitude factor $s = 7$, which corresponds to a growth in amplitude of $\exp(s) \approx 10^3$ according to the definition in eq. (83). This suggests that deep channels were probably formed through reactive, rather than shear-driven instability. This would only be reinforced by inclusion of volatile-driven reactive melting (Keller & Katz 2016).

5.2 Orientation dependence of growth

We now turn our attention to the consequences of wavevector orientation. Fig. 10 shows a set of four models, plotted in terms of accumulated growth of the perturbation. In each case, we set the perturbation wavevector to have orientation θ_0 as it enters the melting region from below. The wavevector then evolves along streamlines of the corner flow. The left-hand column shows the total growth s_{total} , which is the sum of the growth from reaction s_{reaction} (middle column) and the growth from shear s_{shear} (right-hand column). Overall it is evident that accumulated growth is sensitive to the initial orientation.

Row (a) shows that when the initial wavevector is vertical ($\theta_0 = \pi/2$; the porosity bands are initially horizontal), the instability is suppressed. There is contraction across the bands, so the shear-driven instability has a negative growth rate. The bands remain close enough to horizontal that the reactive mode of instability only grows slowly. The net effect is that the overall growth is negative.

Row (b) shows that when the initial wavevector has an angle $\theta_0 = \pi/4$, there is some growth of the instability. Again, there is contraction across the bands, so shear-driven instability has a negative growth rate. The bands also have a larger component in the vertical direction, so the reaction-driven instability is now more significant. In total, the reaction-driven instability is large enough to offset the shear-driven suppression of the instability and give net positive growth.

Row (c) shows that when the initial wavevector is horizontal ($\theta_0 = 0$) and the porosity bands are initially vertical, the instability grows rapidly. These bands start in the orientation most favourable to the reaction-driven instability. However, they are rotated into an orientation with relatively large extension across bands, so the shear-driven instability is also significant. Rotation along streamlines slightly reduces the reactive growth, but this reduction is insignificant. In total, reaction and shear cooperate to drive strong growth of porosity bands.

Row (d) shows that when the initial wavevector has an angle $\theta_0 = -\pi/4$, the instability is partially suppressed. There is some initial growth of both reactive and shear-driven instability. However, following the streamlines, the wavevector is rotated into an orientation where there is very little reactive growth and there is decay caused by contraction across the bands. Thus, in total, by the time the lithosphere is reached, the porosity bands are suppressed.

5.3 Growth with a spectrum of initial wavevector orientations

Fig. 11 considers the evolution of a spectrum of initial wavevector orientations. This is evaluated along two particular streamlines, one near the ridge axis and one further off-axis, shown by the dashed curves in Fig. 7(d). At the base of the melting region, independent of position θ_0 , we assume that the initial magnitude of the wavevector is uniformly distributed, that is, independent of θ_0 . The spectrum

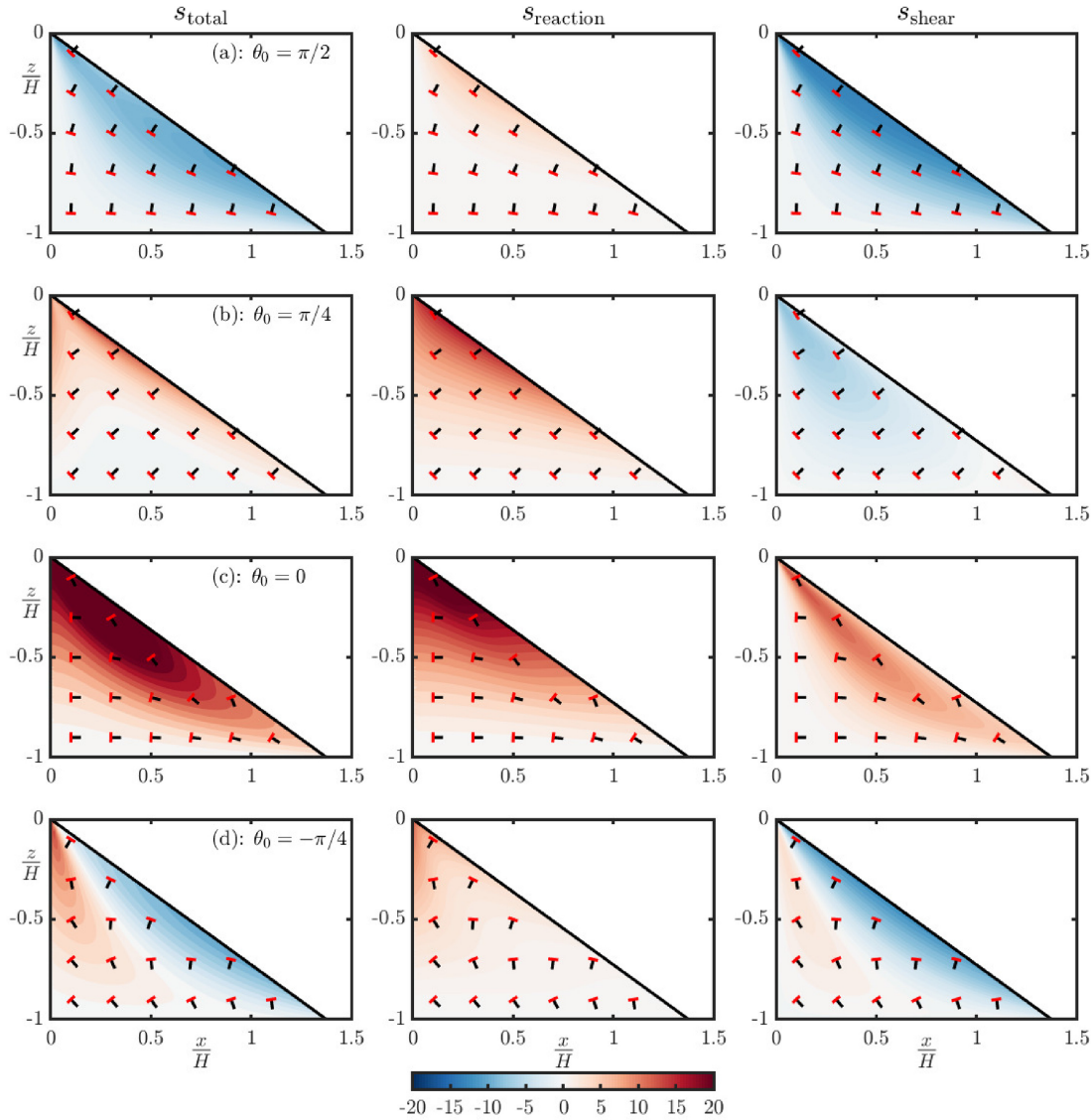


Figure 10. The growth of instabilities initialized with a single wavevector orientated with row: (a) $\theta_0 = \pi/2$; (b) $\theta_0 = \pi/4$; (c) $\theta_0 = 0$; (d) $\theta_0 = -\pi/4$. The left-hand column shows the total growth s_{total} which is the sum of the growth from reaction s_{reaction} (middle column) and the growth from shear s_{shear} (right-hand column). The colour-scale is the same for all panels (and the range is clipped). Black line segments show the orientation of the wavevector and red line segments show the corresponding porosity bands, which are perpendicular to the wavevector.

is then evolved along streamlines. We plot the final accumulated growth and final wavevector angle for two particular streamlines, attained when these streamlines terminate at the lithosphere.

Row (a) shows results for a streamline near the ridge axis. Here, the reactive growth favours wavevectors orientated very close to horizontal (vertical porosity bands). The shear-driven instability favours wavevectors orientated with slightly positive initial angle for reasons discussed above. The overall growth favours a wavevector orientation that is intermediate between these angles. The final orientation θ_1 associated with the greatest accumulated growth is rotated by the shear flow. So high-porosity bands might be expected to correspond to a final wavevector orientation in the pale yellow shaded region range, roughly $-\pi/2 < \theta_1 < 0$.

Row (b) shows results for a streamline further from the ridge axis. The results are similar to row (a). The only important difference is that reactive growth favours wavevectors orientated with a slightly positive initial angle. This is because such bands accumulate more

reactive growth as they are rotated clockwise into the vertical orientation by the shear. For this example, the overall growth favours an initial wavevector angle that is very similar to that favoured by both reaction-driven growth and shear-driven growth separately, with the peak s occurring at a very similar angle for each mechanism. Further calculations (not shown) find similar patterns of behaviour even further off-axis, so the results in row (b) are illustrative of the general pattern away from the immediate vicinity of the ridge axis (row a).

Fig. 12 shows the evolution of perturbations that have maximal ultimate growth over all initial orientations θ_0 . This maximum is evaluated for each streamline separately, with the aim of highlighting the perturbations that would be most likely expressed in a full, non-linear solution (albeit the full non-linear solution may behave differently, as discussed in Section 6.2). An alternative approach is to optimize over the initial wavevector orientation independently at each point in the interior of the melting region, rather than just

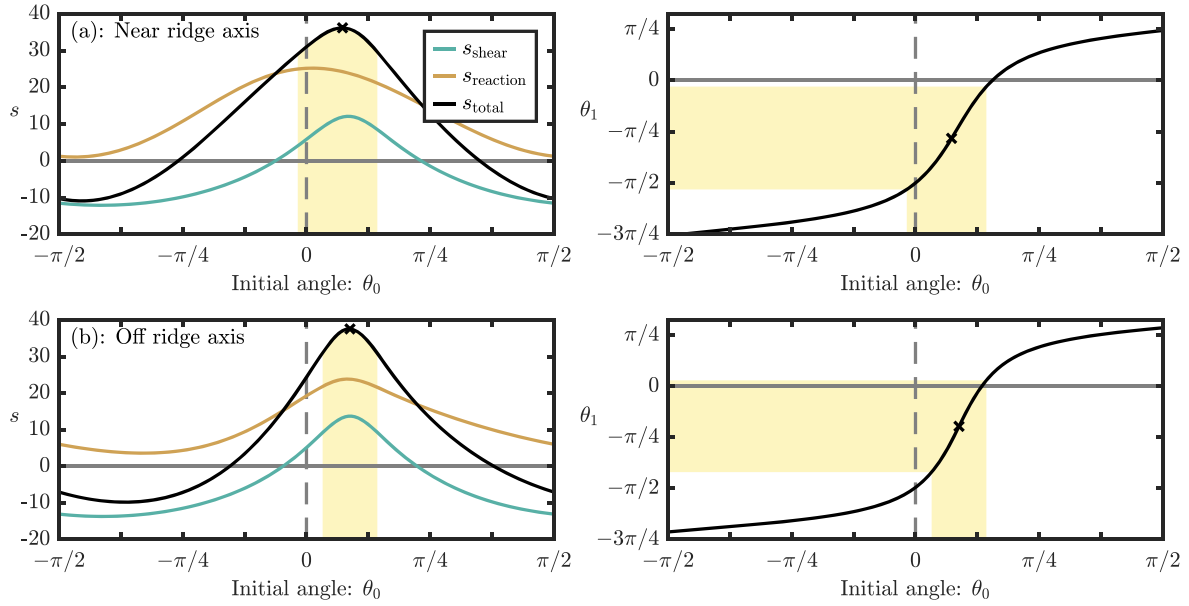


Figure 11. The effect of the orientation of the wavevector θ_0 on the total accumulated growth s at the end of a streamline (left-hand column) and orientation of the final wavevector θ_1 (right-hand column). A black cross marks the most unstable initial wavevector orientation. The pale yellow shaded region highlights wavevector orientations with a total growth within 80 per cent of the maximum. The top row (a) is an example for a streamline near the ridge axis $\tilde{x}_0 = 0.01$ and the bottom row (b) is an example for a streamline further from the ridge axis $\tilde{x} = 0.2$. These streamlines are shown as dashed magenta curves in Fig. 7(d).

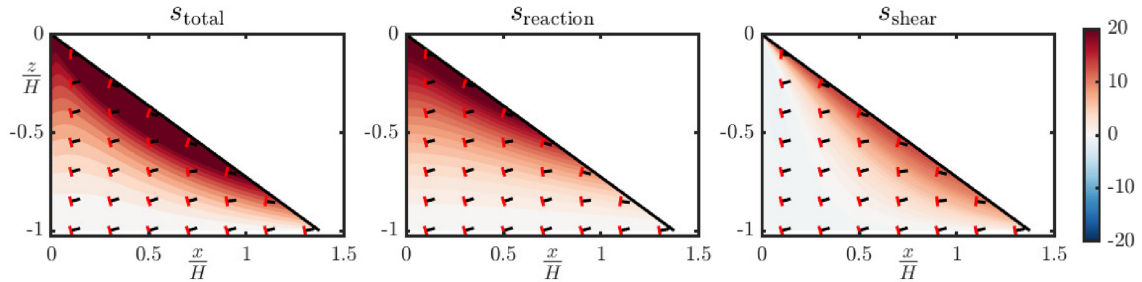


Figure 12. The evolution of the most unstable initial orientation of the wavevector from the bottom row of Fig. 11. Other figure details are as in Fig. 10.

at the end of each streamline. We present calculations using this alternative approach in Appendix B.

Fig. 12 demonstrates that the most unstable orientation varies only slightly with distance off the axis. At every location, the most unstable wavevector is close to horizontal and the corresponding porosity bands are close to vertical. The calculations reinforce the point that was discussed when considering the upper bound on growth shown in Fig. 9—that all channels are initially formed by the reactive mode of instability, and that axial channels are dominated by reactive growth. In this case, shear actually reduces the growth for the deeper part of the streamline. For off-axis streamlines, shear contributes to the growth of instability as the streamlines approach the lithosphere. However, the roots of channels are always associated with reactive rather than shear-driven instability.

5.4 Parametric sensitivity

Fig. 13 shows that this emphasis on the importance of reactive instability is robust to changes in the parameters considered. In row (a), the ratio of bulk to shear viscosity is increased to $\xi_0/\eta_0 = 10$, which is six times higher than the reference case. This has

the effect of suppressing the shear-driven mode of instability, such that the total accumulated growth is dominated by reaction throughout the melting region. Consequently, the most unstable orientation of the wavevector is close to horizontal, since this produces the vertical, high porosity channels favoured by reaction. The solid flow still plays a role in rotating the wavevector. In row (b), we show that a similar pattern is obtained by increasing the relative magma flow speed Q_0/U_0 by a factor of 10, which corresponds to a maximum melt speed of 13 myr^{-1} . This increases the reactive growth rate rather than decreasing the shear-driven growth rate, but the relative effect is the same as for variations in the viscosity ratio (note the different colour scale). The only situation that allows shear to play a greater role is when the bulk-to-shear viscosity ratio is low (as in the reference case) and the melt velocity is also low. For this case, taking Q_0/U_0 as 16 times smaller than the reference case, which corresponds to a maximum melt speed of 1 myr^{-1} , row (c) shows that in most of the domain, shear is more important than reaction. Very close to the ridge axis, reaction remains dominant. However, as we discussed in Section 4.1.3, this segregation rate is probably too slow to satisfy observational constraints. Thus, under more realistic choices of parameters, our model predicts that reaction-driven instability plays the dominant role.

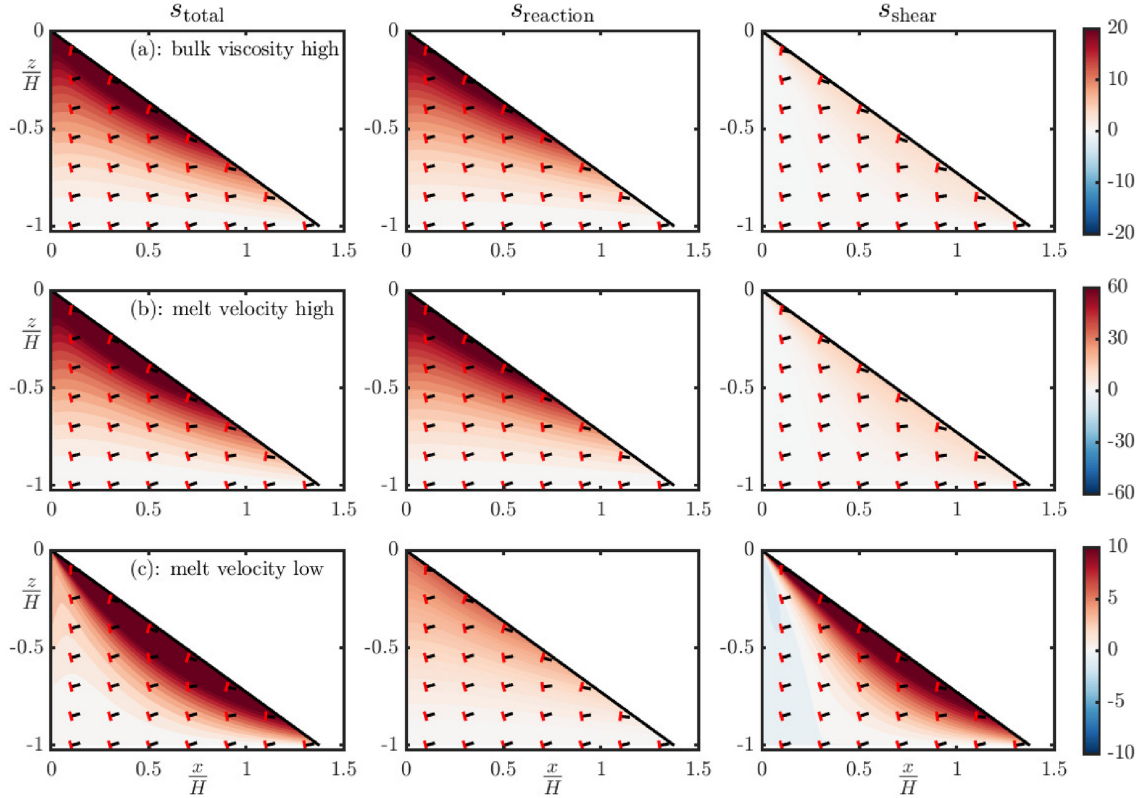


Figure 13. Sensitivity experiments showing the results with the optimal initial wavevector orientation. Row (a) has a higher bulk-to-shear viscosity ratio $\zeta_0/\eta_0 = 10$, which is six times larger than the reference case. Row (b) has a higher melt velocity ratio $Q_0/U_0 = 6.3 \times 10^6$, which is 10 times greater than the reference case. Row (c) has a lower melt velocity ratio $Q_0/U_0 = 4 \times 10^3$, which is 16 times smaller than the reference case. Note the different colour scales. Other figure details are as in Fig. 12.

In Fig. 14 we consider a reduced lithospheric slope, such as might correspond to a faster spreading rate. The results are more complex than in the reference geometry, so we plot them for a set of different initial wavevector orientation to explore this complexity (as in fig. 10). The pattern of reaction-driven growth is similar to calculations with a more steeply dipping lithospheric base. This is as expected, given that it is not directly sensitive to the strain-rate field. However, the pattern of shear-driven growth differs, especially in rows (b) and (c). In row (b), we find a positive contribution to the instability from shear as the streamlines approach the lithosphere, whereas the equivalent contribution in Fig. 10(b) was slightly negative. Conversely, in row (c), we find a slightly negative contribution whereas the equivalent contribution in Fig. 10(c) was positive. These differences reflect the different orientation of strain rate that results when the base of the lithosphere has a shallower dip. Nevertheless, the overall picture of a reactive instability that dominates the dynamics and favours subvertical high-porosity channels persists under these conditions.

6 DISCUSSION

6.1 Summary of results

The results above investigate channelized melt extraction from the mantle and the combined role of two known mechanisms of flow localization, reaction- and shear-driven instability. The theoretical framework developed in Section 2 allows us to simultaneously describe these two mechanisms in a manner consistent with published

results obtained separately for the reaction-infiltration instability and the shear-driven instability. In Section 3, we showed that the relative importance of shear-driven versus reaction-driven instability is governed by the dimensionless ratio given in eq. (51), which we rewrite here:

$$S = \frac{\sigma_{\text{shear}}}{\sigma_{\text{reaction}}} = \frac{2\lambda^*}{n \left(\frac{4}{3} + \frac{\zeta_0}{\eta_0} \right)} \frac{\alpha}{\beta} \frac{\dot{\gamma}_0}{w_0}. \quad (92)$$

The ratio S represents the ratio of growth rates due to shear and due to reaction. S is controlled by a particular combination of mechanical material properties

$$2\lambda^* n^{-1} \left(\frac{4}{3} + \frac{\zeta_0}{\eta_0} \right)^{-1},$$

the reactivity of the system β/α (which has units of m^{-1}), the background rate of melt flow w_0 , and the background solid strain rate $\dot{\gamma}_0$. The dimensionless parameter S is distinct from both the ‘Fiji’ number

$$\Phi g = \frac{\Delta \rho g}{\frac{\eta_0 \dot{\gamma}_0}{0.3\delta}} \quad (93)$$

and the Damköhler number discussed in the review of Kohlstedt & Holtzman (2009). The parameter Φg is related to the ratio of shear-driven melt velocity to buoyancy-driven melt velocity and would come into the imaginary part of the growth rate. The imaginary part is associated with porosity waves; here we chose to focus on the real part of the growth rate, which controls the amplitude of porosity bands. The Damköhler number controls the degree of disequilibrium. We showed that this plays only a modest role in

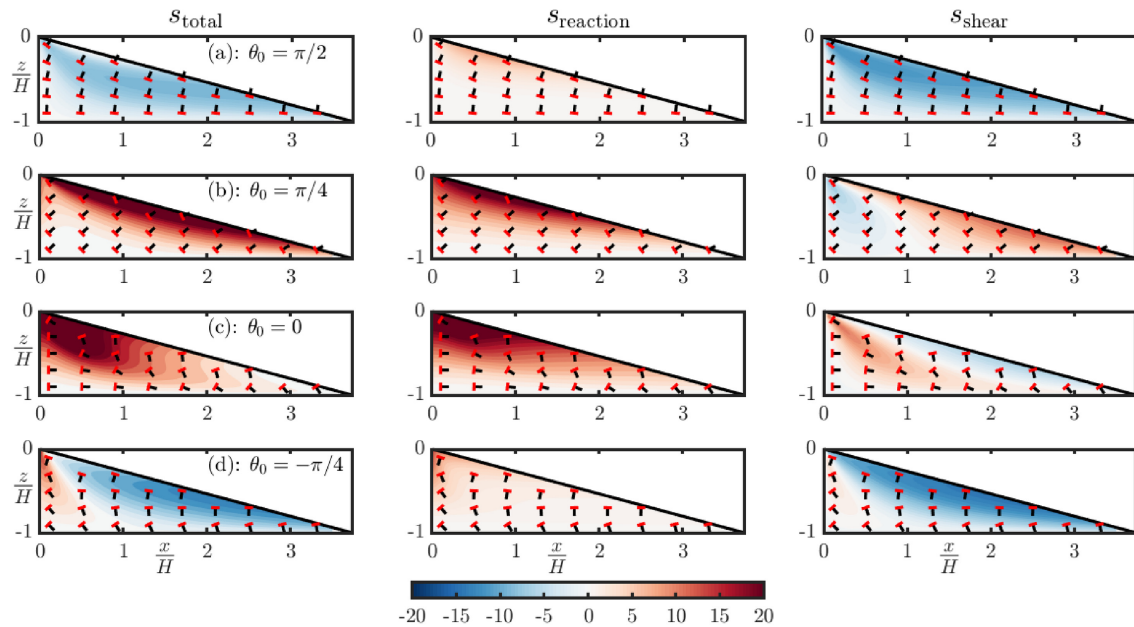


Figure 14. Sensitivity experiment with a shallower dip $\pi/12$ of the lithospheric base showing a range of initial wavevector orientations. Other figure details are as in Fig. 10.

affecting the overall growth rate; instead, the crucial parameter is the reactivity β/α , which appears in S .

The definition of S highlights the crucial role played by the material properties of partially molten rocks, some of which are not well constrained. Indeed, there remain important differences between micromechanical models. Perhaps the greatest uncertainty is the case of the bulk viscosity, as demonstrated by the contrast between model predictions (Takei & Holtzman 2009a,b; Simpson *et al.* 2010; Rudge 2018). As a consequence of these uncertainties, robust, leading-order features of laboratory experiments (e.g. Holtzman & Kohlstedt 2007) such as the orientation of high-porosity bands, their size, spacing and rate of emergence remain challenging to predict quantitatively (Alisic *et al.* 2016). Because of this gap in our knowledge, we face significant uncertainty in extrapolating between the laboratory scale and the mantle scale. The laboratory experiments are performed in closed capsules with a fixed melt fraction deforming at very high strain rates, whereas the MOR system is open to melt flow and deforms a million times more slowly. In this context, we have opted for the simplest form of model that captures the shear-driven formation of porosity bands. In particular, we have not considered a power-law shear viscosity (Katz *et al.* 2006), anisotropic viscosity (Takei & Katz 2015; Qi *et al.* 2015), or the stabilizing influence of surface tension (Parsons *et al.* 2008; King *et al.* 2011a; Bercovici & Rudge 2016). Our methodology could be extended to include these effects, but such extensions are most worthwhile once there is a more settled and complete understanding of the shear-driven formation of porosity bands in isolation.

Our results also clarify the geometric controls on the combined instability. The reaction-infiltration instability has only one preferred direction in the context of our model—the vertical. This is because the background magma flow direction and the solubility gradient are aligned with gravity. In the absence of shear, there is rotational symmetry about the vertical, so the instability leads to the formation of tube-shaped regions of elevated porosity. The presence of a large-scale, solid shear flow breaks this symmetry. Provided the deviatoric stress in the horizontal direction is extensional rather than contractional, even a small amount of shear favours the formation

of tabular, high-porosity bands (Section 3.2). This situation applies at a MOR, for example. The orientation of the resulting bands is intermediate between that favoured by reaction (vertical) and that favoured by shear, and is controlled by the parameter S . Thus the tabular geometry of dunite bodies in ophiolites is consistent with a reactive origin combined with extension in the horizontal direction. The favoured orientation is only weakly affected by considering the full pressure-dependence of the solubility gradient that drives the reaction infiltration instability (see Appendix A, Fig. A1). Nonetheless, the pressure dependence of the solubility gradient may be important in the nonlinear development of channels, particularly in the presence of strong lateral pressure gradients. This suggests an important role for numerical models, as discussed in Section 6.3.

We briefly discussed the dependence of the growth rate on wavelength, which is potentially significant in setting the length scale of dunites. Growth is suppressed at length scales that exceed the compaction length, so channels have a smaller scale in the direction of the wavevector than the compaction length, which is thought to be about a kilometre in the mantle. In previous work, we showed that the reaction-infiltration instability can lead to channels growing with a scale consistent with geological observations, within the considerable parametric uncertainty (Braun & Kelemen 2002; Rees Jones & Katz 2018). Given this parametric uncertainty and the incomplete understanding of the length scales of shear-driven porosity bands, it is premature to draw definitive conclusions.

We applied our model of the combined instability to a MOR using the method proposed by Gebhardt & Butler (2016), as described in Section 4. Our results (Section 5) are summarized in Fig. 15, where panels (a)–(c) show the accumulated growth s as a function of depth for three different corner-flow streamlines that ascend from the bottom of the melting region. The contribution of shear (green) is significant only at shallow depths and/or far from the ridge axis. Geochemical evidence requires channels to form at least 15 km beneath the Moho (Kelemen *et al.* 1997) and U-series disequilibrium and reactive-flow models suggest it is possibly much deeper (Jull *et al.* 2002; Keller & Katz 2016; Liu & Liang 2019).

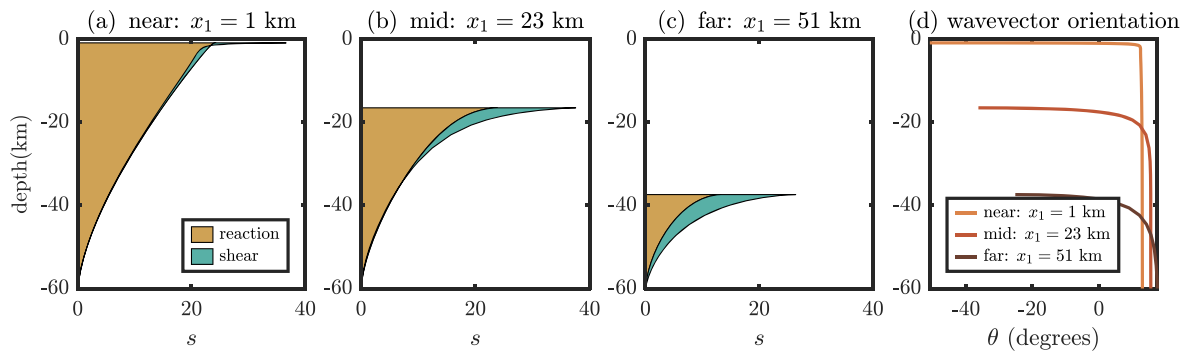


Figure 15. (a–c) The relative and combined importance of reaction (brown) and shear (green) to the amplitude of the porosity bands s . Plots show the evolution along three streamlines that finish at positions x_1 increasingly far from the ridge axis. (d) The rotation of the wavevector along the same three streamlines. Calculations use the reference set of parameters. Cases (a) and (b) correspond to the streamlines plotted in Fig. 11. The conversion to dimensional units is based on $H = 60$ km for illustration.

Together this indicates that instantaneous growth rates are dominated by reaction and affected by shear only along the base of the lithosphere.

Nonetheless, the shear associated with tectonic-scale flow is important in that it promotes the tabular geometry of channels and affects the orientation of channels by rotating their tops away from the ridge axis, which corresponds to a decrease in wavevector angle along the streamline, as shown in Fig. 15(d). Most of this rotation happens very close to the upper end of a streamline, where the streamline turns the corner and terminates at the base of the lithosphere. The most unstable initial orientation of bands is close to vertical, with their tops tilted slightly towards the ridge axis. Bands with this orientation grow rapidly, mainly due to the reactive instability. Near the end of the streamline, the bands are rotated further and can end up lying between the vertical and the horizontal. We explored whether these results are robust to the choice of parameters used, including the angle from the horizontal to the base of the lithosphere. The only combination of parameters that favoured shear over reaction is a very slow melt velocity (≤ 1 m yr $^{-1}$) with a small bulk-to-shear viscosity ratio [$O(1)$]. There is evidence for much more rapid melt extraction ($\gtrsim 10$ m yr $^{-1}$) based on the Icelandic deglaciation (e.g. Jull & McKenzie 1996; MacLennan *et al.* 2002; Eksinhol *et al.* 2019; Rees Jones & Rudge 2020) and U-series data (e.g. Iwamori 1994; Kelemen *et al.* 1997; Jull *et al.* 2002; Stracke *et al.* 2006; Elliott & Spiegelman 2014). Given much more rapid melt extraction, it is most likely that reaction is dominant over shear in general.

6.2 Limitations of analysis

Our calculations, like those of Gebhardt & Butler (2016), rely on a separation of scales between the sub-compaction-length scale of porosity localization (≤ 1 km) and the tectonic scale of the MOR (~ 100 km). This separation arguably enables us to embed our idealized calculation of the local growth rate from Section 3 in tectonic models of MOR magmatism. However, we have not shown that these scales are truly separate and, indeed, there are reasons to question this. For example, local perturbation growth could create a pattern of anisotropic material properties (e.g. permeability, viscosity) that would feedback on the large-scale dynamics. It is also worth noting that the same scale separation presents a severe challenge for numerical models that discretize a 2-D or 3-D space. To capture the interaction between the large and small scales requires

either extremely high grid resolution over a very large domain or a more sophisticated, multiscale approach (e.g. Kevrekidis *et al.* 2003).

The linearity of the current approach is another important limitation. The linearized equations apply rigorously only to the initial stages of channel formation; their formal validity breaks down as the perturbation to the background state grows. Exponential growth cannot continue indefinitely and, instead, the channel amplitude saturates (Spiegelman & Kelemen 2003; Liang *et al.* 2010; King *et al.* 2010). At the same time, the lithological imprint of channelized flow (replacive dunites) is advected and rotated by the mantle flow. Lithological structure may serve to lock in the pattern of reactive channels and limit overprinting by shear-driven growth in contrasting directions. This indicates that 2-D numerical models have an important role to play in understanding the nonlinear evolution of channels, channel coalescence and the overall arrangement of magmatic localization. Unfortunately, such numerical models sometimes fail as the localization becomes more pronounced (e.g. Katz & Takei 2013; Vestrum & Butler 2020), perhaps reflecting our incomplete understanding of the physics of partially molten rocks. Numerical diffusion may also mask behaviour that is expected based on the results obtained here. In one possible example of this, Katz (2010) found that shear-driven porosity bands did not emerge in 2-D simulations of melt transport beneath a MOR, even with exaggerated viscous weakening by porosity. However, Katz & Weatherley (2012) demonstrated that inherited lithological heterogeneity in the mantle can lead to sharp localization of melting and melt transport. And while the chemical heterogeneity imposed in that case may be extreme, models by Keller *et al.* (2017) predicted the emergence of channelized flow due to volatile-rich flux melting beneath a MOR. Our approach based on linearization of the governing equations complements these numerical studies.

Other potentially significant issues relate to the background state about which we linearize. It is probably a good approximation to consider that the solid flow is only minimally affected by the magma flow provided the porosity remains small. However, we used a simple Newtonian viscosity for the solid flow; this could be extended to consider a non-Newtonian or anisotropic viscosity. These effects alter the behaviour of the shear-driven instability, reducing the angle of porosity bands. Nevertheless, the principle remains that the bands grow most rapidly at an angle between that favoured by reaction and that favoured by shear. We also assumed that the magma flow was purely vertical, driven by buoyancy. While this can be the dominant

contribution to magma transport, there are other mechanisms (discussed in the following section) that give rise to a more complex, not purely vertical, pattern of magma flow at MORs.

Another related issue that could modify our predictions for MORs is the background compaction rate associated with melt segregation. If the compaction viscosity is a decreasing function of porosity, background compaction acts to stabilize the system against exponential perturbation growth. Hewitt (2010) showed, in the context of a melting-column model, that this effect is significant if the bulk viscosity has an inverse dependence on porosity. The stabilizing effect is much weaker if the compaction viscosity varies only logarithmically with porosity (Rudge 2018; Rees Jones & Katz 2018). This could be reassessed in the MOR geometry.

6.3 Implications

A leading-order observation about MORs is that the volcanic zone is much narrower (~ 10 km) than the lateral extent of the partially molten region (~ 100 km), which means that melt must be focused laterally towards the ridge axis. Spiegelman & McKenzie (1987) and Morgan (1987) hypothesized that dynamic pressure gradients suck melt towards the ridge. Sparks & Parmentier (1991) and Spiegelman (1993) proposed that melts migrate to the ridge through a sublithospheric decompaction channel. More recently, Turner *et al.* (2017) and Sim *et al.* (2020) have argued for ‘melting-pressure focusing’ associated with gradients in compaction pressure. In addition to these mechanisms, Katz *et al.* (2006) suggested that shear-driven porosity bands create an effectively anisotropic permeability, and that they have an orientation such this anisotropy focuses melt towards the ridge (see also Morgan 1987; Daines & Kohlstedt 1997; Kohlstedt & Holtzman 2009; Liu & Liang 2019). In contrast, the present calculations indicate that high-porosity channels typically have a subvertical orientation in the region moderately close to the ridge (see Figs 13 and 15d). Beneath the lithosphere, they remain subvertical but tend to rotate away from the ridge axis due to the corner flow. The anisotropic permeability structure that might arise from this pattern would not contribute much to melt focusing. On the other hand, melt focusing by pressure gradients might lead to reaction-induced channels that point towards the ridge axis, aligned with the magmatic flow direction (Rabinowicz & Ceuleneer 2005). Numerical models could be used to test the hypothesis that lateral pressure gradients additionally drive the formation of diagonal reactive dissolution channels through pressure-dependence of the solubility gradient (Appendix A), thereby enhancing focusing (Spiegelman *et al.* 2001).

Coherent alignment of melt within the mantle could give rise to anisotropy of seismic wave speeds. Measured anisotropy might therefore be related to the predictions above if the influence of melt can be disentangled from other causes of anisotropy. Kendall (1994) and Blackman & Kendall (1997) recognized the potential for grain-scale alignment of melt to shape the pattern of anisotropy beneath MORs. Later, Holtzman & Kendall (2010) argued that localized melt-fraction perturbations (channels or bands) would also induce seismic anisotropy. To explain observations of seismic anisotropy beneath some MORs, Holtzman & Kendall (2010) and Nowacki *et al.* (2012) invoke sheets of higher melt fraction subparallel to the lithosphere–asthenosphere boundary (LAB) at some 50 km from the ridge axis to create a tilted transverse isotropy (TTI). While such alignment was predicted by Katz *et al.* (2006) and Holtzman & Kendall (2010) on the basis of the shear-driven instability, results

presented here cast doubt on it and hence on the TTI hypothesis. However, plate spreading at the Main Ethiopian Rift is associated with a fast seismic direction that is ridge-parallel (Kendall *et al.* 2005; Hammond *et al.* 2014). The subvertical, tabular magmatic structures that we predict to arise from the shear-modified reaction-infiltration instability are consistent with such anisotropy. Alignment of magmatic features subparallel to the shallowly dipping LAB may instead arise by the dynamic response to magmatic flow towards an impermeable boundary (Sparks & Parmentier 1991; Hewitt & Fowler 2008). Alternatively, seismic anisotropy may arise from a grain-scale texture [e.g. lattice- or melt-preferred orientation (Holtzman *et al.* 2003b; Qi *et al.* 2018)] rather than accumulated growth of macroscopic localization patterns, as initially proposed by Kendall (1994).

6.4 Conclusions

(i) We developed a consistent framework to model the combined growth of reaction-driven and shear-driven instabilities in the partially molten mantle and calculated their linear growth rate. We applied that framework to the melting region beneath MORs.

(ii) The reactive-infiltration instability is dominant over most of the melting region and, in particular, along its base and close to the ridge axis, where mantle flow is vertical. This gives rise to subvertical, high-porosity channels that form sufficiently deep within the melting region to explain the observed disequilibrium between erupted lavas and the harzburgitic upper mantle.

(iii) The presence of even a small amount of horizontal extension favours tabular channels over tube-shaped channels, consistent with the morphology of observed dunites.

(iv) The shear-driven instability may contribute to further growth of channels along the base of the lithosphere. However, the orientation of these channels is set by prior growth in the reactive-flow regime and hence they remain subvertical, despite some rotation by the corner flow.

(v) Within the limitations of our study, shear-driven melt bands do not function as a mechanism for melt focusing at MORs. Moreover, we predict that bands are not aligned consistently with the shallow-dipping seismic anisotropy that has been obtained by inversions.

ACKNOWLEDGEMENTS

Insightful comments by P. Kelemen and an anonymous reviewer helped us to improve the manuscript. DWRJ acknowledges research funding through the NERC (Natural Environment Research Council) Consortium grant NE/M000427/1. The research of RFK leading to these results received funding under the European Research Council Horizon 2020 research and innovation programme, grant agreement number 772255. We thank the Deep Carbon Observatory of the Alfred P. Sloan Foundation.

DATA AVAILABILITY STATEMENT

Software that implements the theoretical methods presented this article is archived by Zenodo and available at <https://doi.org/10.5281/zenodo.4618182> (Rees Jones *et al.* 2021).

REFERENCES

- Aharonov, E., Whitehead, J.A., Kelemen, P.B. & Spiegelman, M., 1995. Channeling instability of upwelling melt in the mantle, *J. geophys. Res.*, **100**(B10), 20433–20450.

- Alisic, L., Rhebergen, S., Rudge, J.F., Katz, R.F. & Wells, G.N., 2016. Torsion of a cylinder of partially molten rock with a spherical inclusion: theory and simulation, *Geochem. Geophys. Geosyst.*, **17**(1), 143–161.
- Baltzell, C., Parmentier, E.M., Liang, Y. & Tirupathi, S., 2015. A high-order numerical study of reactive dissolution in an upwelling heterogeneous mantle: 2. Effect of shear deformation, *Geochem. Geophys. Geosyst.*, **16**(11), 3855–3869.
- Batchelor, G.K., 1967. *An Introduction to Fluid Mechanics*, Cambridge Univ. Press.
- Bercovici, D. & Rudge, J.F., 2016. A mechanism for mode selection in melt band instabilities, *Earth Planet. Sci. Lett.*, **433**, 139–145.
- Blackman, D.K. & Kendall, J.-M., 1997. Sensitivity of teleseismic body waves to mineral texture and melt in the mantle beneath a mid-ocean ridge, *Phil. Trans. R. Soc. A*, **355**(1723), 217–231.
- Braun, M.G. & Kelemen, P.B., 2002. Dunite distribution in the Oman ophiolite: implications for melt flux through porous dunite conduits, *Geochem. Geophys. Geosyst.*, **3**(11), 1–21.
- Butler, S.L., 2009. The effects of buoyancy on shear-induced melt bands in a compacting porous medium, *Phys. Earth planet. Inter.*, **173**(1–2), 51–59.
- Butler, S.L., 2010. Porosity localizing instability in a compacting porous layer in a pure shear flow and the evolution of porosity band wavelength, *Phys. Earth planet. Inter.*, **182**, 30–41.
- Butler, S.L., 2012. Numerical models of shear-induced melt band formation with anisotropic matrix viscosity, *Phys. Earth planet. Inter.*, **200–201**, 28–36.
- Connolly, J.A.D., Schmidt, M.W., Solferino, G. & Bagdassarov, N., 2009. Permeability of asthenospheric mantle and melt extraction rates at mid-ocean ridges, *Nature*, **462**(7270), 209–212.
- Daines, M. & Kohlstedt, D., 1997. Influence of deformation on melt topology in peridotites, *J. geophys. Res.*, **102**, 10 257–10 271.
- Eksinichol, I., Rudge, J.F. & MacLennan, J., 2019. Rate of melt ascent beneath Iceland from the magmatic response to deglaciation, *Geochem. Geophys. Geosyst.*, **20**(6), 2585–2605.
- Elliott, T. & Spiegelman, M., 2014. Melt migration in oceanic crustal production: a U-series perspective, in *Treatise on Geochemistry*, 2nd edn, pp. 543–581, eds Holland, H.D. & Turekian, K.K., Elsevier.
- Gebhardt, D.J. & Butler, S.L., 2016. Linear analysis of melt band formation in a mid-ocean ridge corner flow, *Geophys. Res. Lett.*, **43**(8), 3700–3707.
- Ghods, A. & Arkani-Hamed, J., 2000. Melt migration beneath mid-ocean ridges, *Geophys. J. Int.*, **140**, 687–697.
- Hammond, J. O.S., Kendall, J.-M., Wookey, J., Stuart, G.W., Keir, D. & Ayele, A., 2014. Differentiating flow, melt, or fossil seismic anisotropy beneath Ethiopia, *Geochem., Geophys., Geosyst.*, **15**(5), 1878–1894.
- Hesse, M.A., Schiemenz, A.R., Liang, Y. & Parmentier, E.M., 2011. Compaction-dissolution waves in an upwelling mantle column, *Geophys. J. Int.*, **187**(3), 1057–1075.
- Hewitt, I.J., 2010. Modelling melting rates in upwelling mantle, *Earth Planet. Sci. Lett.*, **300**, 264–274.
- Hewitt, I.J. & Fowler, A.C., 2008. Partial melting in an upwelling mantle column, *Phil. Trans. R. Soc. Lond., A*, **464**, 2097, doi:10.1098/rspa.2008.0045.
- Hirschmann, M.M., Asimow, P.D., Ghiorso, M.S. & Stolper, E.M., 1999. Calculation of peridotite partial melting from thermodynamic models of minerals and melts. III. Controls on isobaric melt production and the effect of water on melt production, *J. Petrol.*, **40**(5), 831–851.
- Holtzman, B.K. & Kendall, J.-M., 2010. Organized melt, seismic anisotropy, and plate boundary lubrication, *Geochem. Geophys. Geosyst.*, **11**(12), doi:10.1029/2010GC003296.
- Holtzman, B.K. & Kohlstedt, D., 2007. Stress-driven melt segregation and strain partitioning in partially molten rocks: effects of stress and strain, *J. Petrol.*, **48**, 2379–2406.
- Holtzman, B.K., Groebner, N.J., Zimmerman, M.E., Ginsberg, S.B. & Kohlstedt, D.L., 2003a. Stress-driven melt segregation in partially molten rocks, *Geochem. Geophys. Geosyst.*, **4**(5), doi:10.1029/2001GC000258.
- Holtzman, B.K., Kohlstedt, D.L., Zimmerman, M.E., Heidelbach, F., Hiraga, T. & Hustoft, J., 2003b. Melt segregation and strain partitioning: implications for seismic anisotropy and mantle flow, *Science*, **301**, 1227–1230.
- Iwamori, H., 1994. 238U–230Th–226Ra and 235U–231Pa disequilibria produced by mantle melting with porous and channel flows, *Earth planet. Sci. Lett.*, **125**(1–4), 1–16.
- Jordan, J.S. & Hesse, M.A., 2015. Reactive transport in a partially molten system with binary solid solution, *Geochem. Geophys. Geosyst.*, **16**(12), 4153–4177.
- Jull, M. & McKenzie, D., 1996. The effect of deglaciation on mantle melting beneath Iceland, *J. geophys. Res.*, **101**, 21 815–21 828.
- Jull, M., Kelemen, P. & Sims, K., 2002. Consequences of diffuse and channelled porous melt migration on uranium series disequilibria, *Geochim. Cosmochim. Acta*, **66**(23), 4133–4148.
- Katz, R.F., 2010. Porosity-driven convection and asymmetry beneath mid-ocean ridges, *Geochem. Geophys. Geosyst.*, **11**(11), doi:10.1029/2010GC003282.
- Katz, R.F. & Takei, Y., 2013. Consequences of viscous anisotropy in a deforming, two-phase aggregate: 2. Numerical solutions of the full equations, *J. Fluid Mech.*, **734**, 456–485.
- Katz, R.F. & Weatherley, S.M., 2012. Consequences of mantle heterogeneity for melt extraction at mid-ocean ridges, *Earth planet. Sci. Lett.*, **335–336**, 226–237.
- Katz, R.F., Spiegelman, M. & Holtzman, B., 2006. The dynamics of melt and shear localization in partially molten aggregates, *Nature*, **442**, 676–679.
- Kawakatsu, H., Kumar, P., Takei, Y., Shinohara, M., Kanazawa, T., Araki, E. & Suyehiro, K., 2009. Seismic evidence for sharp lithosphere–asthenosphere boundaries of oceanic plates, *Science*, **324**(5926), 499–502.
- Kelemen, P.B., 1990. Reaction between ultramafic rock and fractionating basaltic magma I. Phase relations, the origin of calc-alkaline magma series, and the formation of discordant dunite, *J. Petrol.*, **31**(1), 51–98.
- Kelemen, P.B., Dick, H. J.B. & Quick, J.E., 1992. Formation of hartzburgite by pervasive melt rock reaction in the upper mantle, *Nature*, **358**(6388), 635–641.
- Kelemen, P.B., Shimizu, N. & Salters, V. J.M., 1995a. Extraction of mid-ocean-ridge basalt from the upwelling mantle by focused flow of melt in dunite channels, *Nature*, **375**(6534), 747–753.
- Kelemen, P.B., Whitehead, J.A., Aharonov, E. & Jordahl, K.A., 1995b. Experiments on flow focusing in soluble porous-media, with applications to melt extraction from the mantle, *J. geophys. Res.*, **100**, 475–496.
- Kelemen, P.B., Hirth, G., Shimizu, N., Spiegelman, M. & Dick, H. J.B., 1997. A review of melt migration processes in the adiabatically upwelling mantle beneath oceanic spreading ridges, *Phil. Trans. R. Soc. Lond., A*, **355**(1723), 283–318.
- Kelemen, P.B., Braun, M. & Hirth, G., 2000. Spatial distribution of melt conduits in the mantle beneath oceanic spreading ridges: observations from the Ingalls and Oman ophiolites, *Geochem. Geophys. Geosyst.*, **1**(7), doi:10.1029/1999GC000012.
- Keller, T. & Katz, R.F., 2016. The role of volatiles in reactive melt transport in the asthenosphere, *J. Petrol.*, **57**(6), 1073–1108.
- Keller, T., Katz, R.F. & Hirschmann, M.M., 2017. Volatiles beneath mid-ocean ridges: deep melting, channelised transport, focusing, and metasomatism, *Earth planet. Sci. Lett.*, **464**, 55–68.
- Kendall, J.-M., 1994. Teleseismic arrivals at a mid-ocean ridge: effects of mantle melt and anisotropy, *Geophys. Res. Lett.*, **21**(4), 301–304.
- Kendall, J.-M., Stuart, G.W., Ebinger, C.J., Bastow, I.D. & Keir, D., 2005. Magma-assisted rifting in Ethiopia, *Nature*, **433**(7022), 146–148.
- Kevrekidis, I.G., Gear, C.W., Hyman, J.M., Kevrekidis, P.G., Runborg, O. & Theodoropoulos, C., 2003. Equation-free, coarse-grained multiscale computation: enabling microscopic simulators to perform system-level analysis, *Commun. Math. Sci.*, **1**(4), 715–762.
- King, D. S.H., Zimmerman, M.E. & Kohlstedt, D.L., 2010. Stress-driven melt segregation in partially molten olivine-rich rocks deformed in torsion, *J. Petrol.*, **51**, 21–42.
- King, D. S.H., Hier-Majumder, S. & Kohlstedt, D.L., 2011a. An experimental study of the effects of surface tension in homogenizing perturbations in melt fraction, *Earth Planet. Sci. Lett.*, **307**(3–4), 349–360.
- King, D. S.H., Holtzman, B.K. & Kohlstedt, D.L., 2011b. An experimental investigation of the interactions between reaction-driven and stress-driven

- melt segregation: 1. Application to mantle melt extraction, *Geochem. Geophys. Geosyst.*, **12**(12), doi:10.1029/2011GC003684.
- King, D. S.H., Holtzman, B.K. & Kohlstedt, D.L., 2011c. An experimental investigation of the interactions between reaction-driven and stress-driven melt segregation: 2. Disaggregation at high melt fraction, *Geochem. Geophys. Geosyst.*, **12**(12), doi:10.1029/2011GC003685.
- Kohlstedt, D.L. & Holtzman, B.K., 2009. Shearing melt out of the Earth: an experimentalist's perspective on the influence of deformation on melt extraction, *Ann. Rev. Earth planet. Sci.*, **37**, 561–593.
- Langmuir, C.H., Klein, E. & Plank, T., 1992. Petrological systematics of mid-oceanic ridge basalts: constraints on melt generation beneath ocean ridges, in *Mantle Flow and Melt Generation at Mid-Ocean Ridges*, Vol. 71 of *Geophys. Monogr.*, pp. 183–280, eds Phipps Morgan, J., Blackman, D. & Sinton, J., Am. geophys. Union.
- Liang, Y., Schiemenz, A., Hesse, M.A., Parmentier, E.M. & Hesthaven, J.S., 2010. High-porosity channels for melt migration in the mantle: top is the dunite and bottom is the harzburgite and lherzolite, *Geophys. Res. Lett.*, **37**(15), doi:10.1029/2010GL044162.
- Liu, B. & Liang, Y., 2019. Importance of permeability and deep channel network on the distribution of melt, fractionation of REE in abyssal peridotites, and U-series disequilibria in basalts beneath mid-ocean ridges: a numerical study using a 2D double-porosity model, *Earth planet. Sci. Lett.*, **528**, 115788. doi:10.1016/j.epsl.2019.115788.
- Longhi, J., 2002. Some phase equilibrium systematics of lherzolite melting: I, *Geochem. Geophys. Geosyst.*, **3**(3), 1–33.
- MacLennan, J., Jull, M., McKenzie, D., Slater, L. & Grönvold, K., 2002. The link between volcanism and deglaciation in Iceland, *Geochem. Geophys. Geosyst.*, **3**(11), 1–25.
- McKenzie, D., 1984. The generation and compaction of partially molten rock, *J. Petrol.*, **25**(3), 713–765.
- Mei, S., Bai, W., Hiraga, T. & Kohlstedt, D., 2002. Influence of melt on the creep behavior of olivine-basalt aggregates under hydrous conditions, *Earth planet. Sci. Lett.*, **201**, 491–507.
- Miller, K.J., Zhu, W., Montési, L. G.J. & Gaetani, G.A., 2014. Experimental quantification of permeability of partially molten mantle rock, *Earth planet. Sci. Lett.*, **388**, 273–282.
- Morgan, J.P., 1987. Melt migration beneath mid-ocean spreading centers, *Geophys. Res. Lett.*, **14**(12), 1238–1241.
- Nowacki, A., Kendall, J.-M. & Wookey, J., 2012. Mantle anisotropy beneath the Earth's mid-ocean ridges, *Earth planet. Sci. Lett.*, **317–318**, 56–67.
- Parsons, R.A., Nimmo, F., Hustoft, J.W., Holtzman, B.K. & Kohlstedt, D.L., 2008. An experimental and numerical study of surface tension-driven melt flow, *Earth planet. Sci. Lett.*, **267**(3–4), 548–557.
- Pec, M., Holtzman, B.K., Zimmerman, M.E. & Kohlstedt, D.L., 2015. Reaction infiltration instabilities in experiments on partially molten mantle rocks, *Geology*, **43**(7), 575–578.
- Pec, M., Holtzman, B.K., Zimmerman, M.E. & Kohlstedt, D.L., 2017. Reaction infiltration instabilities in mantle rocks: an experimental investigation, *J. Petrol.*, **58**(5), 979–1003.
- Pec, M., Holtzman, B.K., Zimmerman, M.E. & Kohlstedt, D.L., 2020. Influence of lithology on reactive melt flow channelization, *Geochem. Geophys. Geosyst.*, **21**(8), doi:10.1029/2020GC008937.
- Qi, C., Kohlstedt, D., Katz, R.F. & Takei, Y., 2015. An experimental test of the viscous anisotropy hypothesis for partially molten rocks, *Proc. Nat. Acad. Sci.*, **112**(41), 12 616–12 620.
- Qi, C., Hansen, L.N., Wallis, D., Holtzman, B. K.K. & Kohlstedt, D.L., 2018. Crystallographic preferred orientation of olivine in sheared partially molten rocks: the source of the “a-c switch”, *Geochem., Geophys., Geosyst.*, **160**(B2), 63.
- Quick, J.E., 1982. The origin and significance of large, tabular dunite bodies in the Trinity peridotite, northern California, *Contrib. Mineral. Petrol.*, **78**(4), 413–422.
- Rabinowicz, M. & Ceuleneer, G., 2005. The effect of sloped isotherms on melt migration in the shallow mantle: a physical and numerical model based on observations in the oman ophiolite, *Earth planet. Sci. Lett.*, **229**(3–4), 231–246.
- Rees Jones, D.W. & Katz, R.F., 2018. Reaction-infiltration instability in a compacting porous medium, *J. Fluid Mech.*, **852**, 5–36.
- Rees Jones, D.W. & Rudge, J.F., 2020. Fast magma ascent, revised estimates from the deglaciation of Iceland, *Earth planet. Sci. Lett.*, **542**, 116324.
- Rees Jones, D.W., Katz, R.F. & Zhang, H., 2021. Supporting software code, doi:10.5281/zenodo.4618182.
- Ribe, N.M., 1985. The generation and composition of partial melts in the Earth's mantle, *Earth planet. Sci. Lett.*, **73**(2), 361–376.
- Rudge, J.F., 2018. Textural equilibrium melt geometries around tetrakaidehedral grains, *Proc. R. Soc., A*, **474**(2212), doi:10.1098/rspa.2017.0639.
- Rudge, J.F., 2018. The viscosities of partially molten materials undergoing diffusion creep, *J. geophys. Res.*, **123**(12), 10 534–10 562.
- Schiemenz, A., Liang, Y. & Parmentier, E.M., 2011. A high-order numerical study of reactive dissolution in an upwelling heterogeneous mantle—I. Channelization, channel lithology and channel geometry, *Geophys. J. Int.*, **186**(2), 641–664.
- Sim, S.J., Spiegelman, M., Stegman, D.R. & Wilson, C., 2020. The influence of spreading rate and permeability on melt focusing beneath mid-ocean ridges, *Phys. Earth planet. Inter.*, **304**, 106486.
- Simpson, G., Spiegelman, M. & Weinstein, M.I., 2010. A multiscale model of partial melts: 2. Numerical results, *J. geophys. Res.*, **115**(B4), doi:10.1029/2009JB006376.
- Sims, K.W.W. *et al.*, 2002. Chemical and isotopic constraints on the generation and transport of magma beneath the East Pacific Rise, *Geochim. Cosmochim. Acta*, **66**, 3481–3504.
- Sparks, D.W. & Parmentier, E.M., 1991. Melt extraction from the mantle beneath spreading centers, *Earth. planet. Sci. Lett.*, **105**(4), 368–377.
- Spiegelman, M., 1993. Physics of melt extraction: theory, implications, and applications, *Phil. Trans. R. Soc. Lond., A*, **342**.
- Spiegelman, M., 2003. Linear analysis of melt band formation by simple shear, *Geochem. Geophys. Geosyst.*, **4**(9), doi:10.1029/2002GC000499.
- Spiegelman, M. & Kelemen, P.B., 2003. Extreme chemical variability as a consequence of channelized melt transport, *Geochem. Geophys. Geosyst.*, **4**(7), 1055.
- Spiegelman, M. & McKenzie, D., 1987. Simple 2-D models for melt extraction at mid-ocean ridges and island arcs, *Earth planet. Sci. Lett.*, **83**(1–4), 137–152.
- Spiegelman, M., Kelemen, P.B. & Aharonov, E., 2001. Causes and consequences of flow organization during melt transport: the reaction infiltration instability in compactible media, *J. geophys. Res.*, **106**(B2), 2061–2077.
- Stevenson, D.J., 1989. Spontaneous small-scale melt segregation in partial melts undergoing deformation, *Geophys. Res. Lett.*, **16**(9), 1067–1070.
- Stracke, A., Bourdon, B. & McKenzie, D., 2006. Melt extraction in the Earth's mantle: constraints from U-Th-Pa-Ra studies in oceanic basalts, *Earth planet. Sci. Lett.*, **244**, 97–112.
- Szymczak, P. & Ladd, A. J.C., 2013. Interacting length scales in the reactive-infiltration instability, *Geophys. Res. Lett.*, **40**(12), 3036–3041.
- Szymczak, P. & Ladd, A. J.C., 2014. Reactive-infiltration instabilities in rocks. Part 2. Dissolution of a porous matrix, *J. Fluid Mech.*, **738**, 591–630.
- Tait, S., Jahrling, K. & Jaupart, C., 1992. The planform of compositional convection and chimney formation in a mushy layer, *Nature*, **359**(6394), 406–408.
- Takei, Y., 1998. Constitutive mechanical relations of solid-liquid composites in terms of grain-boundary contiguity, *J. geophys. Res.*, **103**, 18 183–18 203.
- Takei, Y. & Holtzman, B.K., 2009a. Viscous constitutive relations of solid-liquid composites in terms of grain boundary contiguity: 1. Grain boundary diffusion control model, *J. geophys. Res.*, **114**(B6), doi:10.1029/2008JB005850.
- Takei, Y. & Holtzman, B.K., 2009b. Viscous constitutive relations of solid-liquid composites in terms of grain boundary contiguity: 2. Compositional model for small melt fractions, *J. geophys. Res.*, **114**(B6), doi:10.1029/2008JB005851.
- Takei, Y. & Holtzman, B.K., 2009c. Viscous constitutive relations of solid-liquid composites in terms of grain boundary contiguity: 3. Causes and consequences of viscous anisotropy, *J. geophys. Res.*, **114**(B6), doi:10.1029/2008JB005852.

- Takei, Y. & Katz, R.F., 2013. Consequences of viscous anisotropy in a deforming, two-phase aggregate: 1. Governing equations and linearised analysis, *J. Fluid Mech.*, **734**, 424–455.
- Takei, Y. & Katz, R.F., 2015. Consequences of viscous anisotropy in a deforming, two-phase aggregate. Why is porosity-band angle lowered by viscous anisotropy? *J. Fluid Mech.*, **784**, 199–224.
- Turner, A.J., Katz, R.F., Behn, M.D. & Keller, T., 2017. Magmatic focusing to mid-ocean ridges: the role of grain-size variability and non-Newtonian viscosity, *Geochem. Geophys. Geosys.*, **18**(12), 4342–4355.
- Vestrum, Z.E. & Butler, S.L., 2020. Effects of ongoing melting and buoyancy on melt band evolution in a compacting porous layer, *Phys. Earth planet. Inter.*, **304**, 106485.
- von Bargen, N. & Waff, H.S., 1986. Permeabilities, interfacial-areas and curvatures of partially molten systems – results of numerical computation of equilibrium microstructures, *J. geophys. Res.*, **91**, 9261–9276.
- Wark, D.A. & Watson, E.B., 1998. Grain-scale permeabilities of texturally equilibrated, monomineralic rocks, *Earth planet. Sci. Lett.*, **164**(3), 591–605.
- Worster, M.G., 1997. Convection in mushy layers, *Ann. Rev. Fluid Mech.*, **29**(1), 91–122.

APPENDIX A: PRESSURE-DEPENDANT REACTIVE MELTING

The reaction-infiltration instability is driven by a chemical solubility gradient. In the main text, we assumed that this gradient was vertical. However, chemical solubility depends not on depth directly but rather on pressure. If the pressure is dominantly lithostatic, then the solubility gradient will be vertical, motivating our assumption in the main text. The purpose of this appendix is to investigate the potential role of pressure-dependent melting by relaxing the assumption that the thermodynamic pressure is dominantly lithostatic. The shear-driven instability creates a pressure gradient that can, in turn, feedback on the reactive instability through the pressure-dependent reactive melt rate. So this appendix allows us to consider another potential mode of coupling between the two types of instability.

We redo the linear stability analysis from Section 2 to account for the full pressure-dependence of the reactive melt rate. To focus on this effect, we strip out other parts of our earlier analysis from the outset. These assumptions led to the simplified growth rate reported in Section 3.1, so we compare with results reported in that section.

A1 Models for pressure-dependent reactive melt rate

We start with the model for the reactive melt rate originally given in eq. (14), which we replace by

$$\mathbf{v}_D \cdot \nabla c_{eq} = \alpha \Gamma, \quad (A1)$$

where we repeated our earlier simplification ($\phi \mathbf{v}_l \approx \mathbf{v}_D$). The solubility gradient ∇c_{eq} plays the role of $\nabla(\beta z)$ earlier. We next assume that the solubility gradient is linearly related to the pressure gradient. Over the full-depth of the melting region this is a simplification, but will be valid locally, consistent with the approach taken in Section 2. Thus

$$\nabla c_{eq} = -m \nabla P_{therm}, \quad (A2)$$

where $m > 0$ is a proportionality constant and ∇P_{therm} denotes the thermodynamic pressure gradient.

The concept of thermodynamic pressure needs to be carefully considered for systems out of equilibrium. Jull & McKenzie (1996) consider two main possibilities, $\nabla P_{therm} = \nabla P_1$ and

$\nabla P_{therm} = \nabla(P_1 - \zeta C)$, in which ∇P_1 is given by eq. (10):

$$\nabla P_1 = 2\mathbf{D}_s \cdot \nabla \eta + \eta \nabla^2 \mathbf{u} + \frac{4}{3} \eta \nabla C + \nabla(\zeta C) + \bar{\rho} \mathbf{g}. \quad (A3)$$

Jull & McKenzie (1996) argue in favour of the second possibility, which corresponds to $-1/3$ times the trace of the solid stress tensor. For the purposes of this appendix, the distinction between these definitions has only a marginal effect on the results, so we consider both possibilities for completeness.

Next, we define the lithostatic pressure gradient

$$\nabla P_{lith} = \bar{\rho} \mathbf{g} \approx \rho_s \mathbf{g} = -\rho_s g \hat{\mathbf{z}}, \quad (A4)$$

where the approximation $\bar{\rho} \approx \rho_s$ is consistent with the assumption $\phi \ll 1$ we made in Section 2. Then we define the non-lithostatic part of the liquid pressure gradient as

$$\nabla P_m = 2\mathbf{D}_s \cdot \nabla \eta + \eta \nabla^2 \mathbf{u} + \frac{4}{3} \eta \nabla C + \nabla(\zeta C), \quad (A5)$$

so

$$\nabla P_l = \nabla P_m + \nabla P_{lith}. \quad (A6)$$

If the thermodynamic pressure is dominated by the lithostatic contribution, then we can combine eqs (A2) and (A4) to obtain $\nabla c_{eq} = m \rho_s g \hat{\mathbf{z}}$, which is consistent with the simplified approach in the main text provided

$$\beta = m \rho_s g \Leftrightarrow m = \frac{\beta}{\rho_s g}. \quad (A7)$$

Finally, we consider the solubility gradient under the two potential definitions of thermodynamic pressure above.

If $\nabla P_{therm} = \nabla P_l$, then

$$\nabla c_{eq} = \beta \left[\hat{\mathbf{z}} - \frac{\nabla P_m}{\rho_s g} \right]. \quad (A8)$$

The dimensionless ratio $\nabla P_m / \rho_s g$ is the additional melting factor arising from consideration of the pressure-dependence of the solubility gradient.

If $\nabla P_{therm} = \nabla(P_l - \zeta C)$, then

$$\nabla c_{eq} = \beta \left[\hat{\mathbf{z}} - \frac{\nabla P_m}{\rho_s g} + \frac{\nabla(\zeta C)}{\rho_s g} \right]. \quad (A9)$$

A2 Revised linear stability analysis

We now redo the linear stability analysis with the generalized reactive melting model. We first rewrite eq. (18) for the Darcy velocity in terms of P_m ,

$$\mathbf{v}_D = K \Delta \rho g \hat{\mathbf{z}} - K \nabla P_m. \quad (A10)$$

As before, this can be decomposed into a base state and perturbation:

$$\mathbf{v}_D = K_0 \Delta \rho g \hat{\mathbf{z}} + \mathbf{v}'_D, \quad (A11)$$

We next expand out the pressure gradient term, making the same simplification that $C_0 = 0$ as in the main text,

$$\begin{aligned} \nabla P'_m &= \nabla P'_l, \\ &= 2\mathbf{D}_0 \cdot \nabla \eta' + \eta_0 \nabla^2 \mathbf{u}' + \left(\frac{4}{3} \eta_0 + \zeta_0\right) \nabla C', \\ &= \nabla \psi' + \left(\frac{4}{3} \eta_0 + \zeta_0\right) \nabla C', \\ &= -2\lambda^* \eta_0 \gamma_0 \nabla \tilde{\psi}' + \left(\frac{4}{3} \eta_0 + \zeta_0\right) \nabla C'. \end{aligned} \quad (A12)$$

Therefore,

$$-K_0 \nabla P'_m = \Lambda \nabla \tilde{\psi}' - \delta^2 \nabla C', \quad (A13)$$

using the definition of δ in eq. (35) and Λ in eq. (36). So

$$\mathbf{v}'_D = n w_0 \hat{\mathbf{z}} \phi' + \Lambda \nabla \tilde{\psi}' - \delta^2 \nabla C'. \quad (\text{A14})$$

As an aside, this gives another interpretation of Λ as a factor that controls the perturbed melt flow arising from the shear-driven instability.

We next linearize the generalized reactive melt rate eq. (A1). Note that the base-state solubility gradient is $\beta \hat{\mathbf{z}}$, independent of the additional terms arising from the pressure-dependence of the solubility gradient. The perturbation to the melt rate is given by

$$\mathbf{v}'_D \cdot \beta \hat{\mathbf{z}} + K_0 \Delta \rho g \hat{\mathbf{z}} \cdot \nabla c'_{\text{eq}} = \alpha \Gamma'. \quad (\text{A15})$$

The extra terms from the pressure-dependence of the solubility gradient depend on the definition of thermodynamic pressure as discussed above. If $\nabla P_{\text{therm}} = \nabla P_l$, we linearize eq. (A8) as follows

$$\nabla c'_{\text{eq}} = \frac{\beta}{\rho_s g} [-\nabla P'_m]. \quad (\text{A16})$$

If $\nabla P_{\text{therm}} = \nabla(P_l - \zeta C)$, we linearize eq. (A9) as follows

$$\nabla c'_{\text{eq}} = \frac{\beta}{\rho_s g} [-\nabla P'_m + \zeta_0 \nabla C']. \quad (\text{A17})$$

From now on, we stick with the latter of these models, seeing that the former can be obtained from it by removing the term coming from $\zeta_0 \nabla C'$.

We next take eq. (A15) and combine it with eqs (A11), (A13) and (A17) to obtain

$$\begin{aligned} \frac{\alpha}{\beta} \Gamma' &= n w_0 \phi' - K_0 \partial_z P'_m + \frac{\Delta \rho}{\rho_s} [-K_0 \partial_z P'_m + K_0 \zeta_0 \partial_z C'], \\ &= n w_0 \phi' - \left(1 + \frac{\Delta \rho}{\rho_s}\right) K_0 \partial_z P'_m + \frac{\Delta \rho}{\rho_s} K_0 \zeta_0 \partial_z C', \\ &= n w_0 \phi' + \left(1 + \frac{\Delta \rho}{\rho_s}\right) (\Lambda \partial_z \tilde{\psi}' - \delta^2 \partial_z C') \\ &\quad + \frac{\Delta \rho}{\rho_s} \zeta_{\text{rel}} \delta^2 \partial_z C', \end{aligned} \quad (\text{A18})$$

where we define

$$\zeta_{\text{rel}} \equiv \frac{1}{1 + \frac{4}{3} \frac{\eta_0}{\zeta_0}} < 1, \quad (\text{A19})$$

such that $\zeta_{\text{rel}} \delta^2 = \zeta_0 K_0$. The difference between the two definitions of thermodynamic pressure amounts to inclusion or exclusion of the term involving ζ_{rel} .

Following the approach of Section 2.2.3 (in which we showed that $\tilde{\psi} = G\tilde{\phi}$), we take normal modes of eq. (A18) as follows:

$$\begin{aligned} \frac{\alpha}{\beta} \tilde{\Gamma} &= n w_0 \tilde{\phi} + \left(1 + \frac{\Delta \rho}{\rho_s}\right) (\Lambda G i k_z \tilde{\phi} - \delta^2 i k_z \tilde{C}) \\ &\quad + \frac{\Delta \rho}{\rho_s} \zeta_{\text{rel}} \delta^2 i k_z \tilde{C}, \\ &= n w_0 \tilde{\phi} + \left(1 + \frac{\Delta \rho}{\rho_s}\right) \Lambda G i k_z \tilde{\phi} \\ &\quad - i k_z \delta^2 \left[1 + \frac{\Delta \rho}{\rho_s} (1 - \zeta_{\text{rel}})\right] \tilde{C}. \end{aligned} \quad (\text{A20})$$

This expression is a generalized version of eq. (40). Next we combine with eqs (38) and (39) in the same way as before to obtain a

generalized expression for the growth rate

$$\begin{aligned} \sigma &= \frac{\beta}{\alpha} n w_0 + \frac{\beta}{\alpha} \left(1 + \frac{\Delta \rho}{\rho_s}\right) i k_z \Lambda G \\ &\quad + \left(1 - \frac{\beta i k_z \delta^2}{\alpha} \left[1 + \frac{\Delta \rho}{\rho_s} (1 - \zeta_{\text{rel}})\right]\right) \\ &\quad \times \frac{\Lambda G k^2 - n w_0 i k_z}{1 + \delta^2 k^2}. \end{aligned} \quad (\text{A21})$$

The additional terms involving $\Delta \rho / \rho_s$ appear in the imaginary part of σ so affect the propagation speed of porosity waves.

We now make the same approximations as in Section 3.1. Throughout this study, we focus on the real part of the growth rate. We also take the large-compaction-length limit ($\delta k \gg 1$). Then

$$\begin{aligned} \text{real}(\sigma) &= \frac{\beta}{\alpha} n w_0 - \frac{\beta}{\alpha} n w_0 \left[1 + \frac{\Delta \rho}{\rho_s} (1 - \zeta_{\text{rel}})\right] \frac{k_z^2}{k^2} \\ &\quad + \frac{\Lambda G}{\delta^2}, \end{aligned} \quad (\text{A22})$$

so

$$\begin{aligned} \text{real}(\sigma) &= \sigma_{\text{reaction}} \left(1 - \left[1 + \frac{\Delta \rho}{\rho_s} (1 - \zeta_{\text{rel}})\right] \frac{k_z^2}{k^2}\right) \\ &\quad + \sigma_{\text{shear}} G. \end{aligned} \quad (\text{A23})$$

We let $\mathcal{R} = \left[1 + \frac{\Delta \rho}{\rho_s} (1 - \zeta_{\text{rel}})\right]$ and note that $k_z = k \sin \theta$. Then

$$\text{real}(\sigma) = \sigma_{\text{reaction}} (1 - \mathcal{R} \sin^2 \theta) + \sigma_{\text{shear}} G. \quad (\text{A24})$$

This is identical to eq. (50) when $\mathcal{R} = 1$. Indeed all the various thermodynamic models of reactive melting can be treated according to the following cases:

$$\mathcal{R} = \begin{cases} 1, & \text{lithostatic only,} \\ 1 + \frac{\Delta \rho}{\rho_s}, & \nabla P_{\text{therm}} = \nabla P_l, \\ 1 + \frac{\Delta \rho}{\rho_s} (1 - \zeta_{\text{rel}}), & \nabla P_{\text{therm}} = \nabla(P_l - \zeta C). \end{cases} \quad (\text{A25})$$

Accounting for the pressure-dependence of the solubility gradient slightly reduces the reactive part of the growth of the instability. However, for partially molten rocks, $\Delta \rho / \rho_s \approx 1.1$. So even for the most different thermodynamic model $\nabla P_{\text{therm}} = \nabla P_l$, \mathcal{R} is only 10 per cent different from the purely lithostatic case. Using $\nabla P_{\text{therm}} = \nabla(P_l - \zeta C)$, reduces this already small difference further, since $\zeta_{\text{rel}} < 1$ and so \mathcal{R} is closer to 1.

Fig. A1 shows that the angular dependence of the growth rate from eq. (A24) is only minimally affected by the choice of \mathcal{R} . In particular, the most unstable orientation satisfies

$$\tan 2\theta = \frac{2S \sin 2\theta_e}{\mathcal{R} + 2S \cos 2\theta_e}, \quad (\text{A26})$$

which is very weakly affected by \mathcal{R} . At small S , the favoured orientation is close to $k_z = 0$ ($\theta = 0$) so the extra stabilization due to $\mathcal{R} > 1$ is unimportant, as shown by eq. (A24). At large S , the growth rate is dominated by shear, so the extra stabilizing of the reactive part of the growth rate is again unimportant, as shown by eq. (A26).

Physically, the pressure-perturbations associated with the shear instability are coupled to the reactive instability through the pressure-dependence of the solubility gradient. However, this coupling only affects the imaginary part of the growth rate. The real part of the growth rate is also affected by pressure perturbations associated with the reactive instability (not the shear-driven instability). Both of these effects are relatively small, because $\Delta \rho / \rho_s \ll 1$.

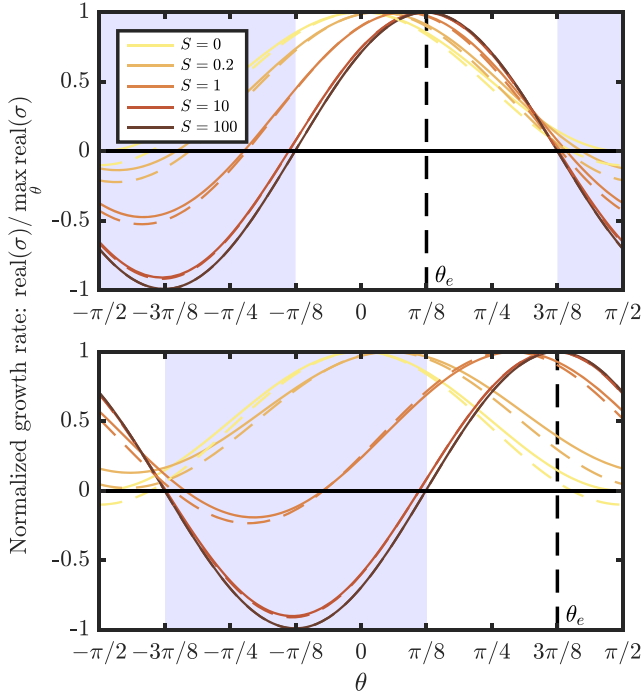


Figure A1. Generalized version of Fig. 3 (see that figure caption for further details). The solid curves correspond to $\mathcal{R} = 1$. The dashed curves correspond to $\mathcal{R} = 1.1$ and hence account for the dependence of the solubility gradient on the dynamic pressure. For the reactive instability only ($S = 0$, yellow curves), the preferred wavevector angle is always $\theta = 0$ corresponding to vertical channels, independent of \mathcal{R} .

This analysis is only preliminary for two reasons. First, the consideration of terms $\Delta\rho/\rho_s$ goes beyond the Boussinesq approximation made throughout this study (see Section 2.1). Secondly, perhaps more importantly, our study is restricted to a linear stability analysis with a vertical base upwelling of magma. So reactive melting is driven by the vertical part of the solubility gradient, which is dominantly lithostatic. In a fully developed nonlinear state, lateral pressure gradients could drive reactive melting and this might be important in understanding the coalescence of channels (Spiegelman *et al.* 2001).

A3 Further considerations for MORs

The importance of the non-lithostatic solubility gradient depends on its magnitude relative to the lithostatic pressure gradient. The latter scales like $\rho_s g$.

Pressure gradients arising from buoyancy-driven flow scale like $\Delta\rho g$, so their relative contribution scales like $\Delta\rho/\rho_s$ —the same scaling we identified in the previous section.

The viscous corner flow (Section 4.1.1) gives rise to a dynamic pressure gradient. This can be estimated from Stokes equation for an incompressible fluid of constant viscosity

$$\nabla P = \eta \nabla^2 \mathbf{u}. \quad (\text{A27})$$

The pressure gradient is singular at the corner ($x = z = 0$ on the diagram in Fig. 6a) and decreases rapidly away from this point. To estimate the scale of this dynamic pressure gradient ∇P_{dyn} , we scale eq. (A27) as follows. We estimate $\eta \sim \eta_0$, $\mathbf{u} \sim U_0$, $\nabla \sim 1/L_{\text{dyn}}$,

where L_{dyn} is the distance from the corner. Then

$$\nabla P_{\text{dyn}} \sim \frac{\eta_0 U_0}{L_{\text{dyn}}^2}. \quad (\text{A28})$$

We then compare this estimate to the lithostatic pressure gradient $\rho_s g$ and find they are comparable when

$$L_{\text{dyn}} \sim \left(\frac{\eta_0 U_0}{\rho_s g} \right)^{1/2} \approx 1 \text{ km}, \quad (\text{A29})$$

where we used the rough estimates $\eta_0 = 10^{19} \text{ Pa s}$, $U_0 = 10 \text{ cm yr}^{-1}$, $\rho_s = 3 \times 10^3 \text{ kg m}^{-3}$ and $g = 10 \text{ m s}^{-2}$. Note that this estimate is factor of $(\Delta\rho/\rho_s)^{1/2}$ smaller than the melt focusing length scale estimated by Spiegelman & McKenzie (1987). In conclusion, within a distance of about a kilometre from the corner, the dynamic pressure gradient is larger than the lithostatic pressure gradient. However, outside this region, the lithostatic pressure gradient is much larger than the dynamic pressure gradient (the latter decreases with the inverse square of distance from the corner). Therefore, we can neglect the contribution of dynamic pressure gradients almost everywhere beneath MORs.

Finally, we estimate the scale of compaction pressure gradients. Turner *et al.* (2017) and Sim *et al.* (2020) have argued for ‘melting-pressure focusing’ associated with gradients in compaction pressure and we base our estimates on these studies. The base state compaction rate C_0 scales like the base state melting rate Γ_0 (ignoring a minus sign), which we estimated in Section 4.1.2. By combining estimates in that section, we find

$$C_0 \sim \Gamma_0 \sim \frac{F_{\text{max}} U_0}{H}. \quad (\text{A30})$$

Then the compaction pressure P_c can be estimated

$$P_c \sim \zeta_0 C_0 \sim \frac{F_{\text{max}} \zeta_0 U_0}{H}. \quad (\text{A31})$$

To estimate the compaction pressure gradient, we must consider the length scale over which the compaction pressure gradient varies. For a triangular melting region an appropriate scale is the depth H , since the width also scales like this. In practice, the length scale is probably somewhat smaller than H (Sim *et al.* 2020), leading to a somewhat higher gradient. Thus

$$\nabla P_c \sim \frac{F_{\text{max}} \zeta_0 U_0}{H^2}. \quad (\text{A32})$$

Finally, we compare this with the lithostatic pressure gradient

$$\frac{\nabla P_c}{\rho_s g} \sim \frac{F_{\text{max}} \zeta_0 U_0}{H^2 \rho_s g} \approx 10^{-3}, \quad (\text{A33})$$

where we used the rough estimates $F_{\text{max}} = 0.2$, $\zeta_0 = 10^{20} \text{ Pa s}$ and $H = 60 \text{ km}$ in addition to the estimates used in eq. (A29). Thus the compaction pressure gradient is a very small fraction of the lithostatic pressure gradient. The same conclusion can be reached by comparing fig. 7 of Sim *et al.* (2020) with the lithostatic pressure $\rho_s g H \approx 2 \times 10^3 \text{ MPa}$.

These arguments do not mean that dynamic and compaction pressure gradients can be neglected when considering melt flow (after all the lithostatic pressure gradient does not drive any flow), only that they can generally be neglected when considering thermodynamic pressure.

APPENDIX B: ALTERNATIVE APPROACH TO WAVEVECTOR OPTIMIZATION FOR MORs

For the main MOR results (Section 5), we optimized the initial wavevector orientation to maximize the total growth accumulated at the end of each streamline. This is relevant if we focus at the location where geological observations of dunite channels are most readily made. However, if we focus on the fabric at depth, it might make more sense to ask what initial wavevector orientation maximizes the total growth at each point in space separately. The results are a little harder to interpret, because the corresponding initial wavevector will not be consistent along each streamline.

Fig. B1 shows the results of this alternative optimization procedure at three different melt segregation speeds. We also plot in the right column the optimal wavevector orientation based on eq. (55),

which reflects the local growth rate. The preferred wavevector orientation is always tilted in a slightly negative orientation (meaning that porosity bands are tilted slightly away from the ridge axis. Near the ridge axis (and across a wide part of the domain in the case of fast melt segregation), the wavevector angle is close to zero and porosity bands are close to vertical. This is because reaction is the dominant mode of instability here. Elsewhere, the wavevector is tilted over at angles up to about $-\pi/4$, with more negative values at slower melt segregation rates. This reflects the relative importance of shear in this case. However, for slower melt segregation, the amplitude of the porosity bands is not very high, especially at depth. The locally most unstable orientation has a similar but distinct pattern (comparing the middle and right columns). It is important, therefore, to track the accumulation of growth and the rotation of the wavevector along streamlines because the most unstable orientation at a particular point cannot be inferred purely from the local behaviour there.

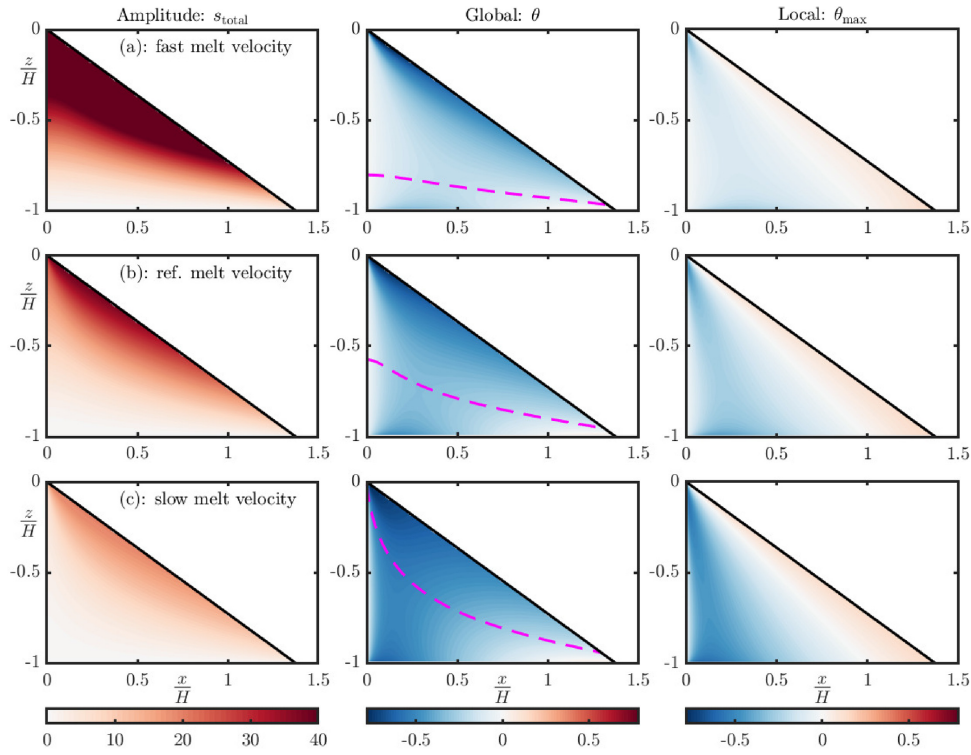


Figure B1. Alternative approach based on optimizing the total growth at each interior point separately, not just at the end of a streamline. The left-hand column shows the amplitude s , the middle column shows the wavevector orientation, the right-hand column shows the optimal orientation in terms of the local growth rate based on eq. (55). We report results at a range of different melt segregation rates. Row (a) has a higher melt velocity ratio $Q_0/U_0 = 6.3 \times 10^6$, which is 10 times greater than the reference case. Row (b) is the reference case. Row (c) has a lower melt velocity ratio $Q_0/U_0 = 4 \times 10^3$, which is 16 times smaller than the reference case. Note the colour scale in (a) is clipped. For the middle column, we added dashed magenta contours of $s_{\text{total}} = 7$. This gives an indication of the level below which the perturbations are very small.